ENGINEERING

Longitudinal intravital imaging of mouse placenta

Xiaoyi Zhu[1]†, Qiang Huang[2,1,3]*†, Laiming Jiang[4,5]†‡, Van-Tu Nguyen[1], Tri Vu[1], Garth Devlin[6], Jabbar Shaima[7], Xiaobei Wang[7], Yong Chen[1]‖, Lijun Ma[1]§, Kun Xiang[1], Ergang Wang[1], Qiangzhou Rong[1], Qifa Zhou[4,5], Yubin Kang[7], Aravind Asokan[6], Liping Feng[8], Shiao-Wen D. Hsu[9], Xiling Shen[1,3]*, Junjie Yao[1]*

Studying placental functions is crucial for understanding pregnancy complications. However, imaging placenta is challenging due to its depth, volume, and motion distortions. In this study, we have developed an implantable placenta window in mice that enables high-resolution photoacoustic and fluorescence imaging of placental development throughout the pregnancy. The placenta window exhibits excellent transparency for light and sound. By combining the placenta window with ultrafast functional photoacoustic microscopy, we were able to investigate the placental development during the entire mouse pregnancy, providing unprecedented spatiotemporal details. Consequently, we examined the acute responses of the placenta to alcohol consumption and cardiac arrest, as well as chronic abnormalities in an inflammation model. We have also observed viral gene delivery at the single-cell level and chemical diffusion through the placenta by using fluorescence imaging. Our results demonstrate that intravital imaging through the placenta window can be a powerful tool for studying placenta functions and understanding the placental origins of adverse pregnancy outcomes.

INTRODUCTION

During pregnancy, the placenta provides nutrients and oxygen to the growing fetus and remove its wastes (*1*, *2*). Dysfunctions in placental development are a common cause of obstetric complications, such as fetal growth restriction (FGR), preterm birth, preeclampsia (PE), and uncontrolled gestational diabetes (*3*). For example, PE occurs in 5 to 8% of pregnancies (up to 200,000 women yearly in the US), and progression to eclampsia causes approximately 13% of all maternal deaths (*4*). The lack of effective treatments of many placenta-related pregnancy diseases is due in part to a paucity of understanding of basic disease mechanisms, particularly the role played by placental hemodynamics.

To this end, many preclinical animal models have been developed for studying the placenta, mostly in mice (*5*–*7*). Mouse and human placentas share similar anatomical, cellular, and molecular features (*8*), and thus, mouse models can be used for longitudinally evaluating the developing placenta (*7*, *9*, *10*). Understanding the mouse placental development under normal and pathological conditions requires in vivo imaging approaches that can measure the hemodynamic functions and molecular activities, as many placenta pathologies are closely related to microvessel remodeling (*11*, *12*) and cellular differentiation (*13*). However, imaging mouse placental functions in vivo is technically challenging because the placenta is deep in the abdominal cavity, has a large size, and is highly mobile due to breathing motion. Existing imaging technologies have various challenges to study in vivo placental development, particularly during early pregnancy. For example, high-resolution ultrasound imaging of microvasculature has been achieved by using power Doppler or microbubble localization (*14*–*19*), but ultrasound molecular imaging is still not broadly applicable outside the vascular space, mostly due to the lack of molecular probes that can be flexibly engineered for various biomedical applications (*20*). Magnetic resonance imaging and x-ray computed tomography lack both the spatial resolution and the molecular sensitivity for mouse placenta study (*21*). High-resolution optical imaging such as two-photon microscopy generally lacks the penetration depth to access the deep-seated placenta (*22*). Thus, innovative imaging technologies with high-resolution, high-speed, and functional and molecular sensitivity are demanded for preclinical research of placental biology.

For high-resolution and longitudinal studies using various optical imaging modalities, intravital imaging techniques via implanted optical windows have been applied to observe biological processes in organs deep inside the abdominal cavity of live animals (*23*, *24*). So far, intravital imaging of mouse placenta with an optical window has not been achieved, mostly due to the placenta's high sensitivity to mechanical stress. Moreover, implanting an optical window on the delicate placenta is a surgical challenge (*25*). In this study, we have developed the first ever intravital placenta window and the corresponding microsurgery procedures to safely access the placenta in situ inside the uterus. The intravital placenta window is optically and acoustically transparent and thus allows for longitudinal optical and ultrasound imaging of the placental development throughout the entire pregnancy.

Moreover, photoacoustic microscopy (PAM) is a hybrid imaging modality that unites light and sound (*26*) and can probe hemodynamic functions and metabolism with a high spatial resolution (*27*–*29*). PAM relies on acoustic detection of the optical absorption

[1]Department of Biomedical Engineering, Duke University, Durham, NC 27708, USA. [2]Department of Pediatric Surgery, Second Affiliated Hospital of Xi'an Jiaotong University, Xi'an, Shaanxi 710004, China. [3]Terasaki Institute for Biomedical Innovation, Los Angeles, CA 90024, USA. [4]Department of Biomedical Engineering, University of Southern California, Los Angeles, CA 90089, USA. [5]Roski Eye Institute, Department of Ophthalmology, Keck School of Medicine, University of Southern California, Los Angeles, CA 90033, USA. [6]Department of Surgery, Duke University School of Medicine, Durham, NC 27708, USA. [7]Division of Hematologic Malignancies and Cellular Therapy, Department of Medicine, Duke University School of Medicine, Durham, NC 27708, USA. [8]Department of Obstetrics and Gynecology, Duke University School of Medicine, Durham, NC 27708, USA. [9]Department of Medicine, Duke University School of Medicine, Durham, NC 27708, USA.
*Corresponding author. Email: qiang.huang@terasaki.org (Q.H.); xiling.shen@terasaki.org (X.S.); junjie.yao@duke.edu (J.Y.)
†These authors contributed equally to this work.
‡Present address: The College of Materials Science and Engineering, Sichuan University, Chengdu 610064, China.
§Present address: Department of Human Anatomy, Histology and Embryology, School of Basic Medicine, Ningxia Medical University, Yinchuan 750004,China.
‖Present address: Department of General Surgery, Xiangya Hospital of Central South University, Changsha, Hunan 410008, China.

contrast (*29*) and provides sensitive blood vessel imaging by using hemoglobin as the endogenous contrast. Therefore, PAM is highly promising for label-free imaging of placental hemodynamics via the intravital placenta window. However, the placenta is very susceptive to breathing motion, and traditional PAM with low imaging speed suffers from severe motion-related distortions. In this study, we have developed the ultrafast functional PAM (UFF-PAM) system, which can simultaneously achieve high imaging speed, large field of view, microvessel-level spatial resolution, and vessel-by-vessel functional analysis (*30*).

Overall, we have developed an imaging technology that can address the outstanding challenges in studying placental hemodynamics and molecular activities. Combining UFF-PAM and the intravital placenta window, our imaging platform has demonstrated longitudinal tracking of the placental hemodynamic signatures in healthy pregnancies. We further tested our imaging system under representative clinical conditions during placentation, including alcohol consumption that induces hyperperfusion and hyperoxia, cardiac arrest (CA) that causes hypoperfusion and hypoxia, and inflammation that results in abnormal microvessel structures and functions. Last, using fluorescence imaging, we also demonstrated longitudinal tracing of placental molecular activities via the placenta window, such as viral gene delivery on the single-cell level and chemical diffusion throughout the placenta.

RESULTS

Intravital placenta window

Implanting an optical window to the developing mouse placenta is technically and surgically challenging, due to its depth in the abdominal cavity, sensitivity to stress, and tight attachment to the embryo (*24*). Here, we have developed the first implantable intravital placenta window. The overall design of the intravital placenta window is shown in Fig. 1(A and B). The assembled window includes three parts: inner window frame (IWF), outer window frame (OWF), and window cap. The IWF is square-shaped with an opening of 10 mm by 10 mm and a thickness of 1.0 mm. During the surgery, IWF is sutured with the abdominal muscle, and the abdominal muscle is sutured to the uterine wall. The abdominal side of IWF has a bevel shape so it can create enough space in between the placenta and window cap, which is critical to avoid mechanical pressure on the developing placenta. After the IWF is implanted, the OWF is mounted to the rim of the IWF. An optically and acoustically transparent membrane (thickness: 10 μm) is attached to OWF to seal the imaging window and protect the placenta from the external environment. OWF can be easily detached from IWF for manipulating the placenta and embryo. OWF also serves as a mounting fixture to the photoacoustic and fluorescence imaging platform, which provides stable support of the placenta window during the imaging. To prevent membrane damage by the mouse gnawing, a window cap is mounted to OWF when the mouse is not in the imaging sessions. The cap can be removed during the imaging procedure. All three window parts are made of biocompatible titanium alloy and do not induce tissue's inflammation response (Fig. 1C). The surgical procedure of implanting the placenta window is summarized in Fig. 1D. Once implanted, the placenta window allows high-resolution photoacoustic and fluorescence imaging of the same placenta longitudinally during the entire pregnancy, without the need for changing the membrane. To reduce the impacts of motion from the dam's breathing, a pair of three-dimensional (3D)–printed clips are used to mount the OWF onto the imaging system.

Impact of intravital placenta window

To determine the potential biological impact of the placenta window implantation on the placenta and embryo development, we implanted the placenta windows on pregnant mice on embryonic day 7.0 (E7.0) and continuously monitored the windows until E19 (Fig. 1E). All the implanted windows lasted throughout the pregnancy. No membrane damage nor skin inflammation was observed. We weighed the mouse embryos placed under the windows at E18.5 and found that embryo weights were reduced by 33.8 ± 8% when compared to the littermates that were not placed under the windows (Fig. 1F). The overall survival rate of the embryos after placenta window implantation was 64.3% (27 of 42). We observed that ~90% of embryo loss (i.e., 32.1% of total embryos) occurred within 24 hours following the window implantation. Thus, we believe that the elevated embryo loss was mostly due to the increased spontaneous resorption rate (pregnancy loss) by the surgical trauma. Naturally, the spontaneous resorption rate is 10 to 20% in mice (*31*). Nevertheless, all the surviving pups under the window developed until birth via natural vaginal delivery at full term, and they showed normal feeding as well (Fig. 1G and movie S1). After giving birth, the dams had normal feeding, grooming, and nesting behavior (movie S2). A month after delivery, the pups under the window had no visual difference compared with their littermates that were not placed under the windows, indicating that the placenta window does not impose long-term impact on the animal development after birth (movie S3).

To further test whether the implanted window caused any structural or functional changes in the dams and embryos, we analyzed hematoxylin and eosin–stained sessions of the placenta and embryos (Fig. 1H and fig. S1, A and B). The histological results showed no structural abnormalities in the embryos and no signs of necrosis in the placenta under the window. A board-certified veterinary pathologist examined sections of placenta isolated by mechanical dissection of the conceptus at E18.5 (fig. S2). No notable degenerative lesions were observed in placental tissues including yolk sac, labyrinth and basal zones, decidua, and metrial gland regions. Further, there were no substantial differences in the whole blood analysis when comparing the embryos under the window to their littermates not under the window (fig. S1C). Similarly, the whole blood analysis in dams showed no signs of inflammation and anemia after the window implantation (fig. S1D). Therefore, we did not observe clear adverse impacts of the intravital placenta window on the development of the placenta and embryos.

Ultrafast functional PAM

Previously, we reported the first-generation UFF-PAM (Gen1-UFF-PAM) system by using a 12-facet water-immersible polygon scanner (Fig. 2A) (*30*). A Raman shifter–based laser system can provide dual-wavelength pulsed excitation at 532 and 558 nm (fig. S3A). The resultant ultrasound waves are received by a spherically focused ring-shaped ultrasound transducer with a central frequency of 40 MHz (Fig. S3B) (*32*). Both the focused excitation light and the resultant ultrasound waves are confocally steered by the water-immersible polygon scanner, and thus, the detection sensitivity can be maintained over the field of view. From the acquired PA signals at the two wavelengths, we can quantify the blood oxygenation level (sO_2) (*28*). We can image the mouse placenta vasculature and sO_2 with a

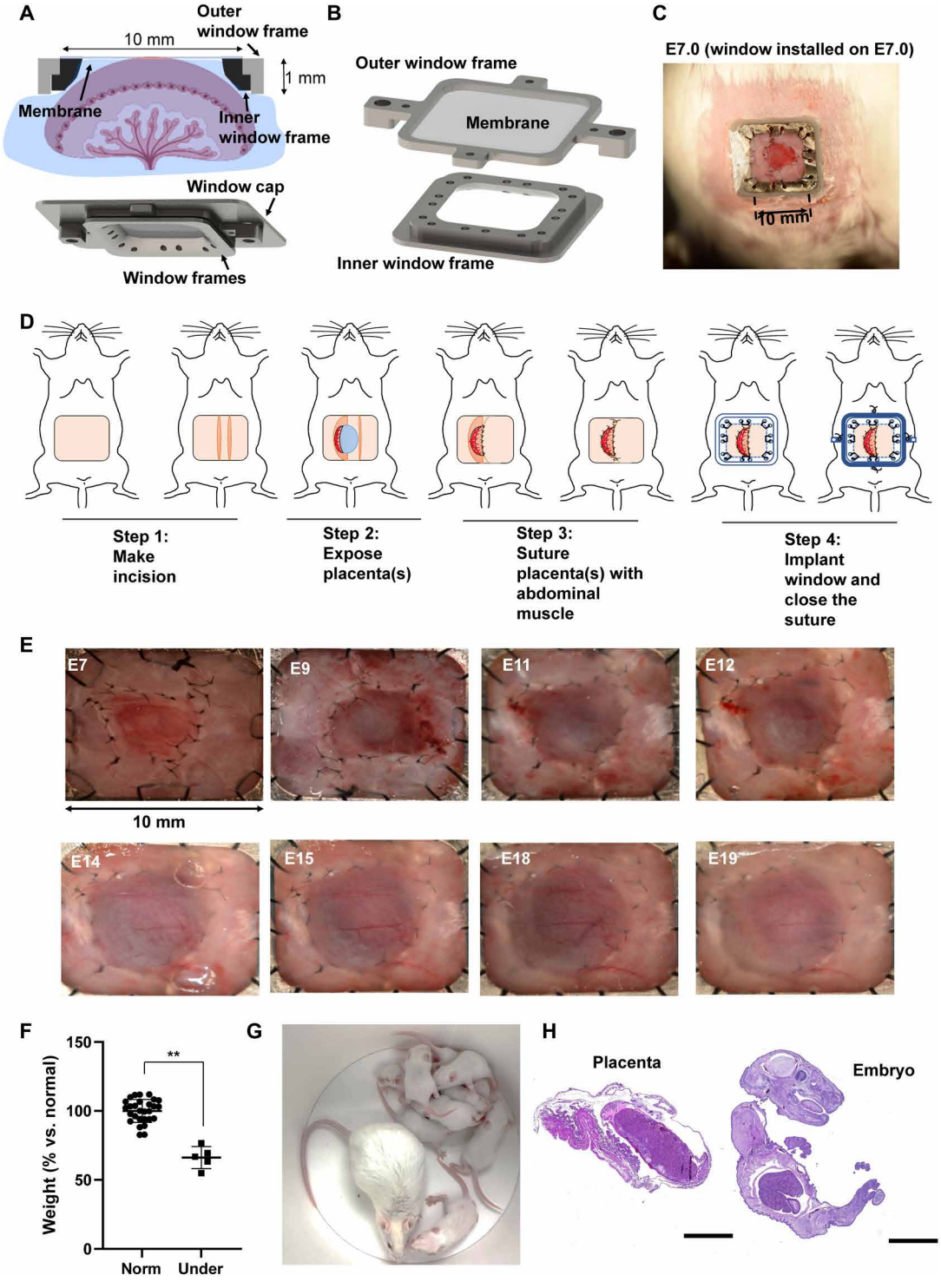

Fig. 1. Intravital placenta window. (**A**) Schematic of the assembled placenta window with the window frames and the window cap. Note the abdominal side of IWF has a bevel shape so it can create enough space in between the placenta and window cap. (**B**) Schematic of two window frames. The IWF secures the placenta during its development, and the OWF provides the imaging access to the placenta with an optically and acoustically transparent membrane. (**C**) Photo of a pregnant mouse at E7.0, with a placenta window installed on E7.0. The window was made of titanium alloy and thus highly compatible with biological tissues. (**D**) Overview of the four key surgical procedures for implanting the placenta window on a pregnant mouse. (**E**) Photos of placenta development from E7 to E19.0 under the placenta window. No signs of tissue inflammation were observed during the pregnancy. (**F**) Weight comparison of the embryos under the placenta window ($N = 5$) and their littermates not under the window ($N = 28$), showing a weight reduction of 33.8%. $^{**}P < 0.01$. (**G**) A month after delivery, the pups under the window had no visual difference compared with their littermates that were not under the windows. (**H**) Hematoxylin and eosin histology of the placenta and embryo under the window, showing no signs of structural necrosis in the placenta and abnormalities in the embryos under the window. Scale bars, 2 mm.

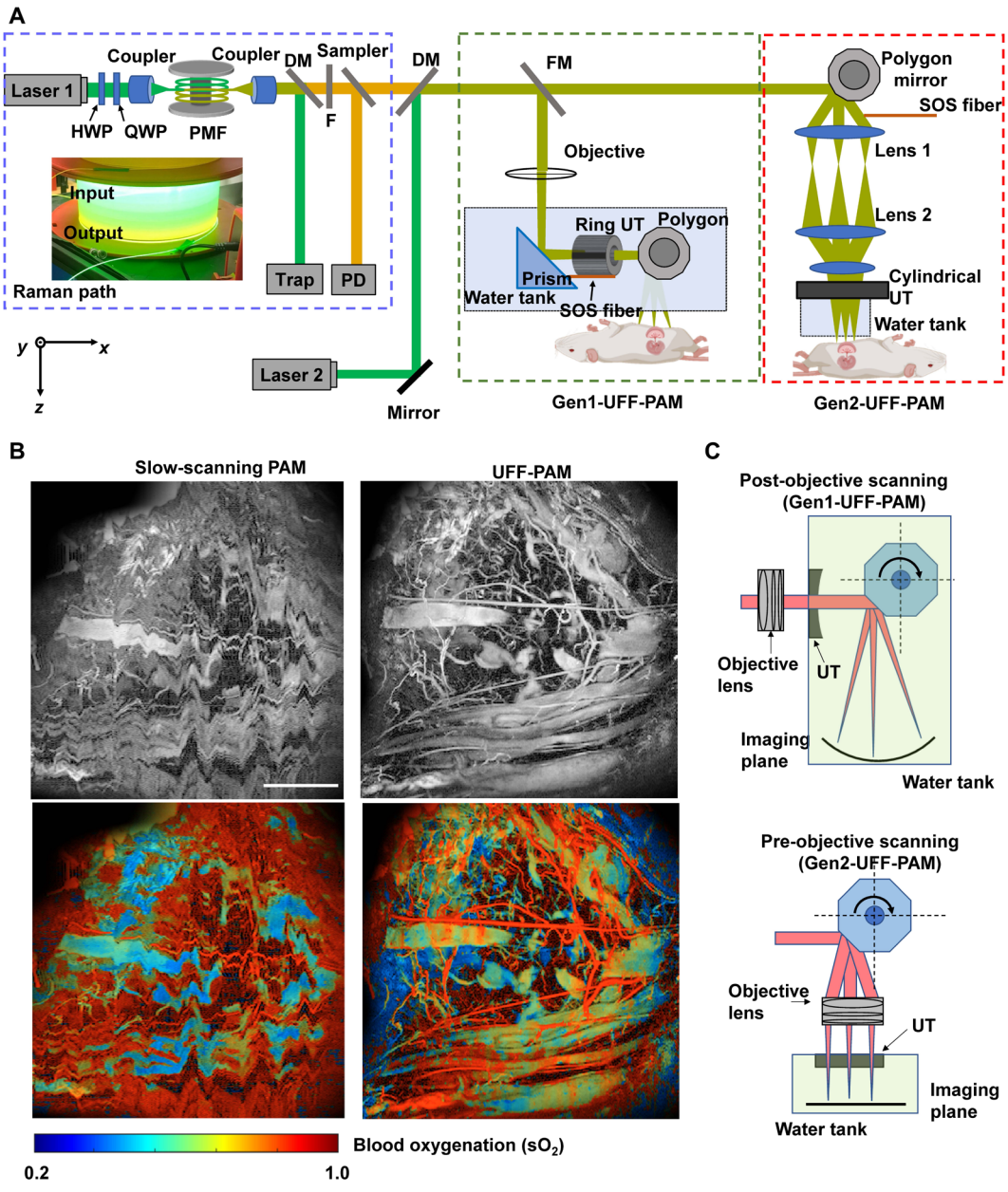

Fig. 2. Ultrafast functional PAM with a large field of view. (**A**) Schematic of two generations of UFF-PAM, with post-objective scanning (Gen1-UFF-PAM) and pre-objective scanning (Gen2-UFF-PAM), respectively. The inset photo shows the laser wavelength shift inside the polarization maintaining fiber of the Raman path. DM, dichroic mirror; FM, flip mirror; HWP, half wave plate; PD, photodiode; PMF, polarization maintaining fiber; QWP, quarter wave plate; SOS, start of scan; UT, ultrasound transducer. (**B**) The comparison of slow-scanning PAM and Gen1-UFF-PAM, showing a representative vasculature image of the mouse placenta along with the corresponding sO_2 map. It took the traditional slow-scanning PAM ~20 min to acquire the image, and as a result, the images suffered from severe motion artifacts induced by animal breathing, such as discontinuous vessels and inaccurate sO_2 quantification. By contrast, it took only 6 s for Gen1-UFF-PAM to acquire the images, which were free of motion artifacts. Scale bar, 1 mm. (**C**) Two generations of UFF-PAM systems, respectively, use the post-objective scanning strategy and the pre-objective scanning strategy. In the Gen1-UFF-PAM, the post-objective scanning strategy is used with a 12-facet water-immersible polygon scanner that steers in water. However, this strategy causes optical aberrations as well as scanning instability, mostly due to the strong water damping force. The Gen2-UFF-PAM system uses a pre-objective scanning strategy, in which the polygon scanner no longer operates in water but instead operates in air.

lateral spatial resolution of ~10 μm and a field of view of 10 mm by 10 mm, which takes only ~6 s. By contrast, the traditional PAM using motorized stages needs ~20 min to image the same field of view and thus suffers from severe motion artifacts induced by animal breathing, including discontinuous vessels and inaccurate sO_2 quantification (Fig. 2B).

A post-objective scanning strategy is used in our Gen1-UFF-PAM, which rotates the polygon scanner at a high speed in water (Fig. 2C). However, high-speed rotation of the polygon in water causes optical aberration as well as scanning instability, mostly due to the strong water damping force. To address this issue, we have developed the second-generation UFF-PAM (Gen2-UFF-PAM)

system with a pre-objective scanning strategy (Fig. 2, A and C), in which the polygon scanner operates in the air (fig. S3C). Doing so, the scanning speed and stability can be improved without water disturbance. The confocal alignment of the excitation light and the acoustic detection is achieved by using a customized cylindrically focused ultrasonic transducer (fig. S4). The acoustic focal line has a length of 10 mm and a width of ~61 μm. The cylindrically focused ultrasonic transducer has a central slit opening that allows the excitation light to pass through. The focused excitation light is steered along the acoustic focal line by the polygon scanner at a line scanning rate up to 3 kHz (fig. S5). Using the Gen2-UFF-PAM, we can image the mouse placenta vasculature and sO_2 with a field of view of 10 mm by 10 mm, which takes only ~0.3 s and is 18 times faster than the Gen1-UFF-PAM.

Moreover, Gen1-UFF-PAM has a curved focal plane with post-objective scanning, which leads to the reduced detection sensitivity toward the ends of the fast-scanning range (fig. S6). Gen2-UFF-PAM uses pre-objective scanning and thus has relatively unform detection sensitivity across the fast-scanning range. Nevertheless, because of the single-dimensional focusing of the cylindrical transducer, Gen2-UFF-PAM has a threefold decrease in averaged detection sensitivity when compared with Gen1-UFF-PAM. In this work, we used both the Gen1- and Gen2-UFF-PAM systems, depending on the required imaging speed by the applications. The detailed imaging parameters used for different experiments are summarized in table S1.

Placental hemodynamics during healthy pregnancy

For the longitudinal imaging of placental development during healthy pregnancy, UFF-PAM was used to track the vasculature and oxygenation changes from E7.0 to E19.0 daily. Benefiting from the large placenta window size (1 cm), we were able to access a single placenta (movie S4) or multiple placentas (Fig. 3A and movie S5) throughout the pregnancy. By quantifying the placenta vasculature morphology (fig. S7) and oxygenation, we made three observations of normal mouse placentation: (i) The averaged vessel diameter increased by 200% from E7.0 to E13.0 (Fig. 3B), primarily due to the remodeling of maternal spiral arteries (*33*). During the early to mid-term placentation, to meet the demands of the developing fetus, the spiral arteries are modified from low flow, high resistance to high flow, low resistance with vasodilation. In the meantime, the fetal vessels were quickly developing in the labyrinth zone. From E13.0 to E19.0, we observed that the averaged vessel diameter decreased by 50% because maternal vascular repair occurred with reendothelialization at term (Fig. 3B) (*34*, *35*). (ii) The averaged vessel density increased monotonically by more than 200% from E7.0 to E15.0 before reaching plateau until E19.0, attributed to the rapid microvessel development in the placenta and embryo during this period. We believe that from the first trimester of the mouse pregnancy to the second trimester, there was a notable escalation in both the quantity and size of placental vessels, which led to increased vessel diameter (Fig. 3B) and vessel density (Fig. 3C). Throughout the third trimester, the development of the placental vasculature persisted. The reduction in vessel diameter during this phase was attributed to the elevated vascular branching (*36*). However, the vascular density remained relatively stable, due to the overall increase in the number of microvessels, despite the decreased vessel diameters (*37*). (iii) The averaged sO_2 first slightly decreased by ~15% from E7.0 to E10.0, indicating a hypoxic environment during the early pregnancy. The low-oxygen condition during this stage is due to the trophoblast plugs that only allow blood plasma to pass through into the intervillous space (*38*, *39*). The low-oxygen environment during early pregnancy helps placental development by promoting angiogenesis and protecting the developing placenta and fetus from oxidative stress (*40*–*42*). The sO_2 increased by ~70% from E10.0 to E15.0 when the trophoblast plugging was less extensive and oxygenated blood was delivered into the interstitial space for exchanging of O_2 and nutrients with the fetal circulation. Then, the sO_2 decreased again by ~17% from E15.0 to E19.0, likely in preparation for delivery. We observed abnormally high sO_2 levels in some major vessel branches during the early trimester, which gradually subsided as the vessels became more mature in the later trimester. Likely due to the vessel remodeling (*43*).

Placental hyperperfusion induced by alcohol consumption

It has been reported that frequent alcohol consumption during pregnancy can have serious and long-term physical, cognitive, and behavioral consequences for the developing fetus, a condition collectively known as fetal alcohol spectrum disorders (FASD) (*44*–*52*). However, the role of placental development in FASD is not well understood (*53*, *54*). Longitudinal monitoring of alcohol consumption during pregnancy may provide the much-needed information on the correlation between placenta development and FASD pathology. To study the acute hemodynamic changes in the placenta after alcohol consumption, we intraperitoneally administered ethanol (3.0 g/kg) into the abdominal cavity of pregnant mice at E12.5 and observed the hemodynamic changes over 10 mins using UFF-PAM (Fig. 4, A and B, and movie S6). Compared with direct oral administration, intraperitoneal administration is conducive to achieving a more controlled and predictable blood alcohol concentration (*55*).

While the average diameter of the placental blood vessels had no notable changes (Fig. 4C), we observed a ~13% increase in the total vessel density within ~100 s after the alcohol consumption (Fig. 4D). The increased vessel density was mainly due to the elevated blood perfusion to the placenta that resulted in recruiting new microvessels otherwise perfused with plasma only (*56*). Moreover, we observed a ~27% increase in the averaged sO_2 of the placenta (Fig. 4E), reflecting elevated blood perfusion and oxygen delivery. The excessive oxygen perfusion lasted for about 3 min, and then the hemodynamics returned to the baseline level. Overall, our results show that alcohol consumption can induce hyperperfusion and elevated levels of oxygenation, which may have detrimental effects on embryonic development (*57*). Specifically, the alcohol-induced hyperoxia can lead to (i) increased oxidative stress within the developing embryo; (ii) neurological damage in the developing brain due to prolonged exposure to oxygen; and (iii) increased risk of preterm delivery due to hyperoxia-induced uterus contractions (*58*). These findings of placenta hemodynamics strongly suggest that alcohol exposure during pregnancy can have harmful effects on fetal development both in the short and long term.

Placental hypoxia in CA

CA during pregnancy is a fatal condition in both pregnant women and their fetuses (*59*–*61*). It is, however, not clear how the placental hemodynamics respond to the CA-induced systemic hypoxia and the following reperfusion. To study the acute hemodynamic responses in the placenta during CA, we applied pure nitrogen for 2 min on the pregnant mice to induce CA and monitored the

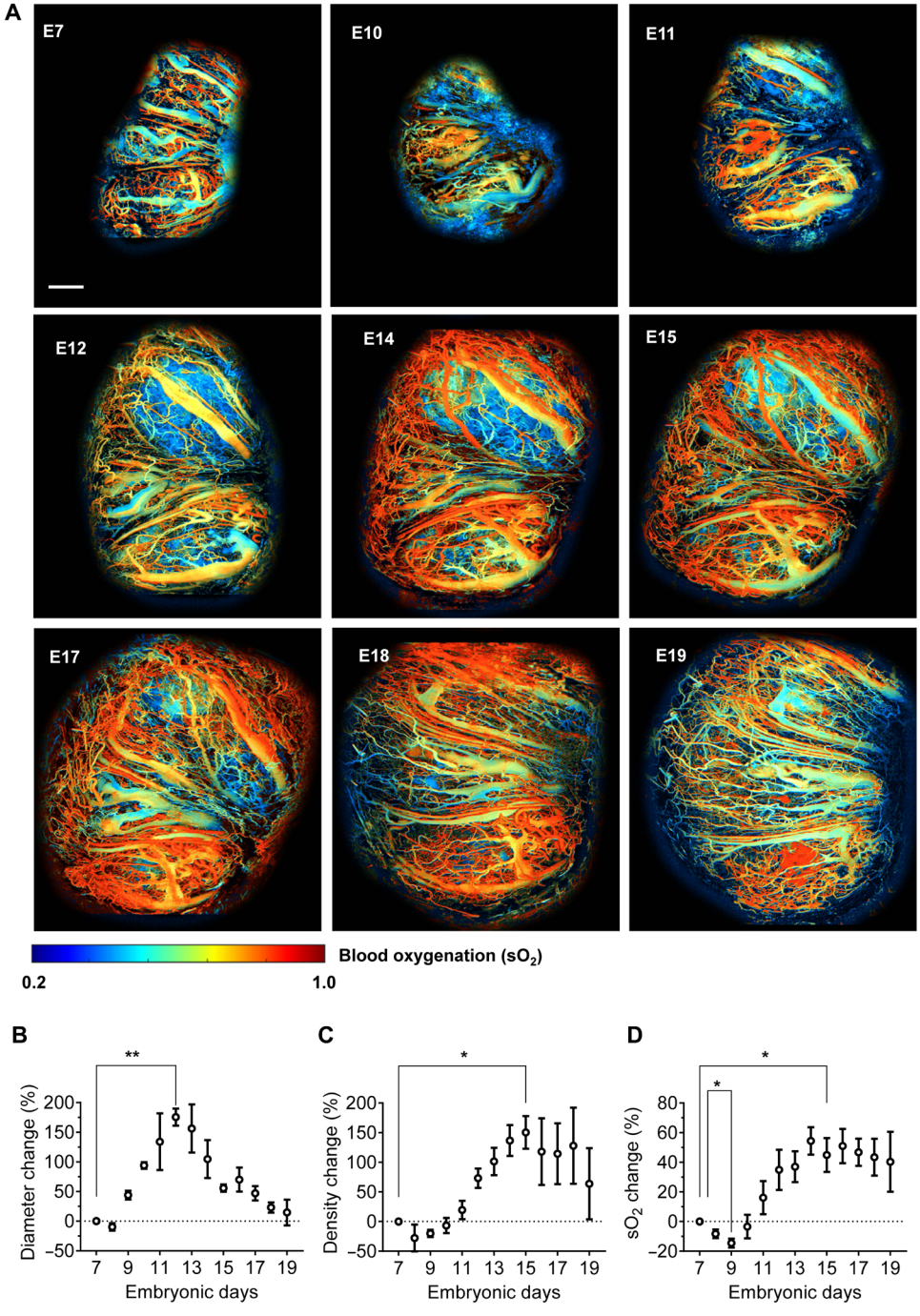

Fig. 3. Longitudinal monitoring of mouse placental hemodynamics throughout a healthy pregnancy. (**A**) Representative UFF-PAM images of the vessel-by-vessel sO_2 mapping of a mouse placenta under the window from E7.0 to E19.0, showing the daily development of placental hemodynamics, such as angiogenesis and vessel remodeling. The placenta window was implemented on E7.0. The transparent placenta window allowed for direct, safe, and longitudinal access to the placenta with microvessel-level spatial resolutions. A total of three placentas were observed simultaneously via the window. Scale bar, 1 mm. (**B**) The placenta vessel diameter change during the healthy pregnancy, showing a monotonic vasodilation up to E12.0 and then a monotonic vasoconstriction to E19.0. (**C**) The vessel density change during the pregnancy, showing a fast microvessel angiogenesis up to E15.0. (**D**) The blood oxygenation (sO_2) change during the pregnancy, showing the hypoxic condition in the early pregnancy up to E9.0, a quick oxygenation increase up to E15.0, and a slight decrease up to E19. $N = 3$ mice. Data are shown in mean ± SEM. * $P < 0.05$; ** $P < 0.01$.

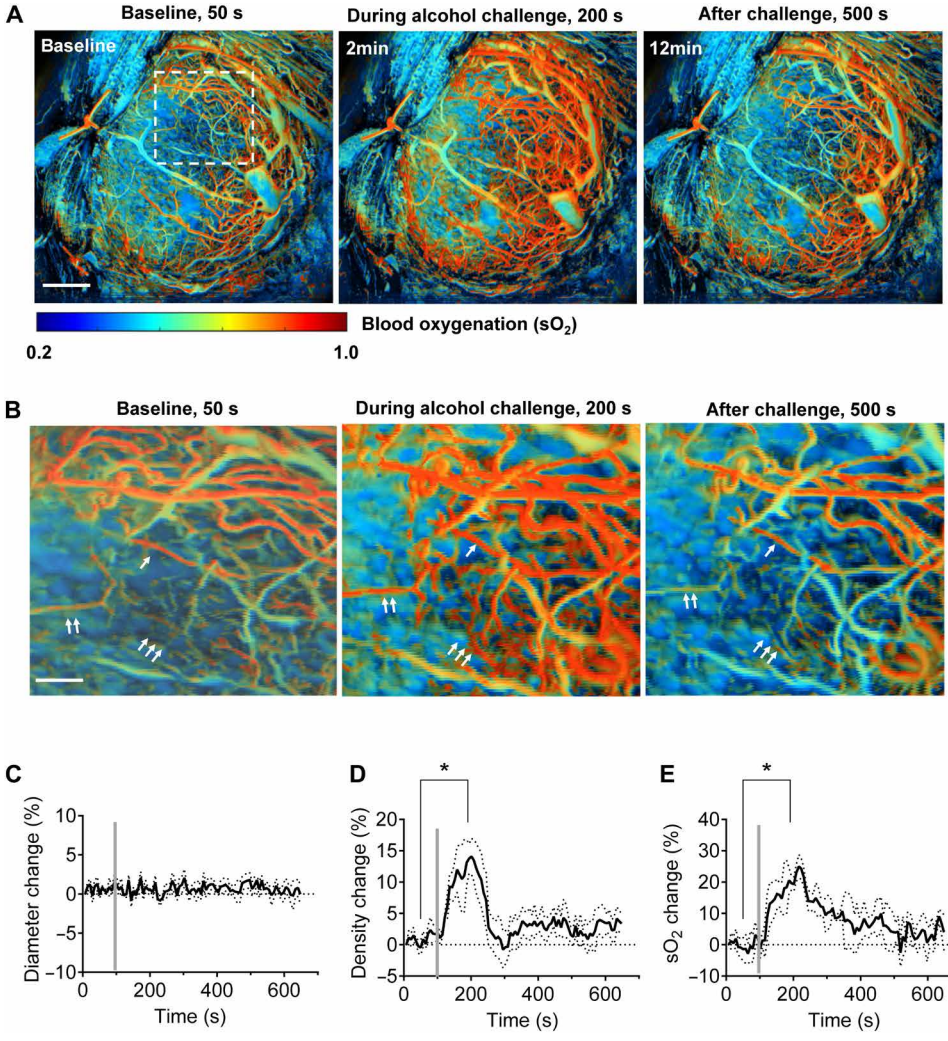

Fig. 4. Rapid placental hemodynamic responses to alcohol consumption. (**A**) Snapshot UFF-PAM sO_2 images of the mouse placenta before, during, and after alcohol consumption, showing clear elevation in the oxygenation induced by the alcohol. The same placenta was continuously monitored for 10 min after the alcohol administration at 100 s. Scale bar, 1 mm. (**B**) Close-up images of the placenta region indicated by the white dashed box in (A), showing the alcohol-induced vessel dilation (single arrow), increased sO_2 level (double arrows), and the elevated blood perfusion in the microvessels (triple arrows). Scale bar, 200 μm. (**C**) The averaged vessel diameters had no substantial changes during the alcohol challenge, a joined effect of vasodilation of existing vessels and the newly recruited microvessels. The gray box represents the starting time of alcohol administration at 100 s. (**D**) The vessel density change induced by the alcohol challenge, showing a clear increase in the vessel density, mostly due to the recruitment of microvessels. (**E**) The blood oxygenation change induced by the alcohol challenge, showing a prolonged hyperoxia condition lasting for ~10 min, mostly due to the elevated blood perfusion. $N = 3$ mice. The data are shown as mean ± SEM. $^*P < 0.05$.

placenta for 25 min using UFF-PAM (Fig. 5A and movie S7). We also recorded the electrocardiogram (ECG) signals of the mouse concurrently with the UFF-PAM measurements (Fig. 5B). Upon the CA challenge, the mouse heart beating rate quickly dropped from 7.3 to 0.25 Hz. There was approximately 45 s delay between the start of the nitrogen challenge and the total onset of CA, which is consistent with our previously published CA model (*62*). Meanwhile, we observed an immediate and substantial reduction in sO_2 across the whole placenta, including both arteries and veins (Fig. 5, C and D). The tissue hypoxia induced vasodilation at a later time point, with an increased vessel diameter by more than 40% on average, mostly due to the increased blood CO_2 level. The recovery of the vessel dilation to the baseline was completed within about 7 min after the treatment (Fig. 5E). The total vessel density had a moderate increase of ~10%, which was a combined outcome of reduced blood perfusion and increased vessel diameters (Fig. 5F). The placental sO_2 decreased immediately after the nitrogen treatment, and the averaged sO_2 was reduced by ~35% during CA. Compared to changes of the vessel diameter and density, the sO_2 drop last much longer, with a total recovery time of >6 min after CA. There was a slight overshot in the sO_2 level at the end of recovery before it returned to the baseline (Fig. 5G). This study presents the first evidence of hemodynamic changes in the placenta following CA. The observed vascular changes suggest that the placenta may compensate for reduced blood flow to the fetus by dilating its vessels during CA. The substantial and instant decrease in sO_2 level indicates rapid oxygen deprivation in the placenta after the CA. Prolonged recovery of sO_2 levels may result in long-term damage to the placenta and fetus (*63*).

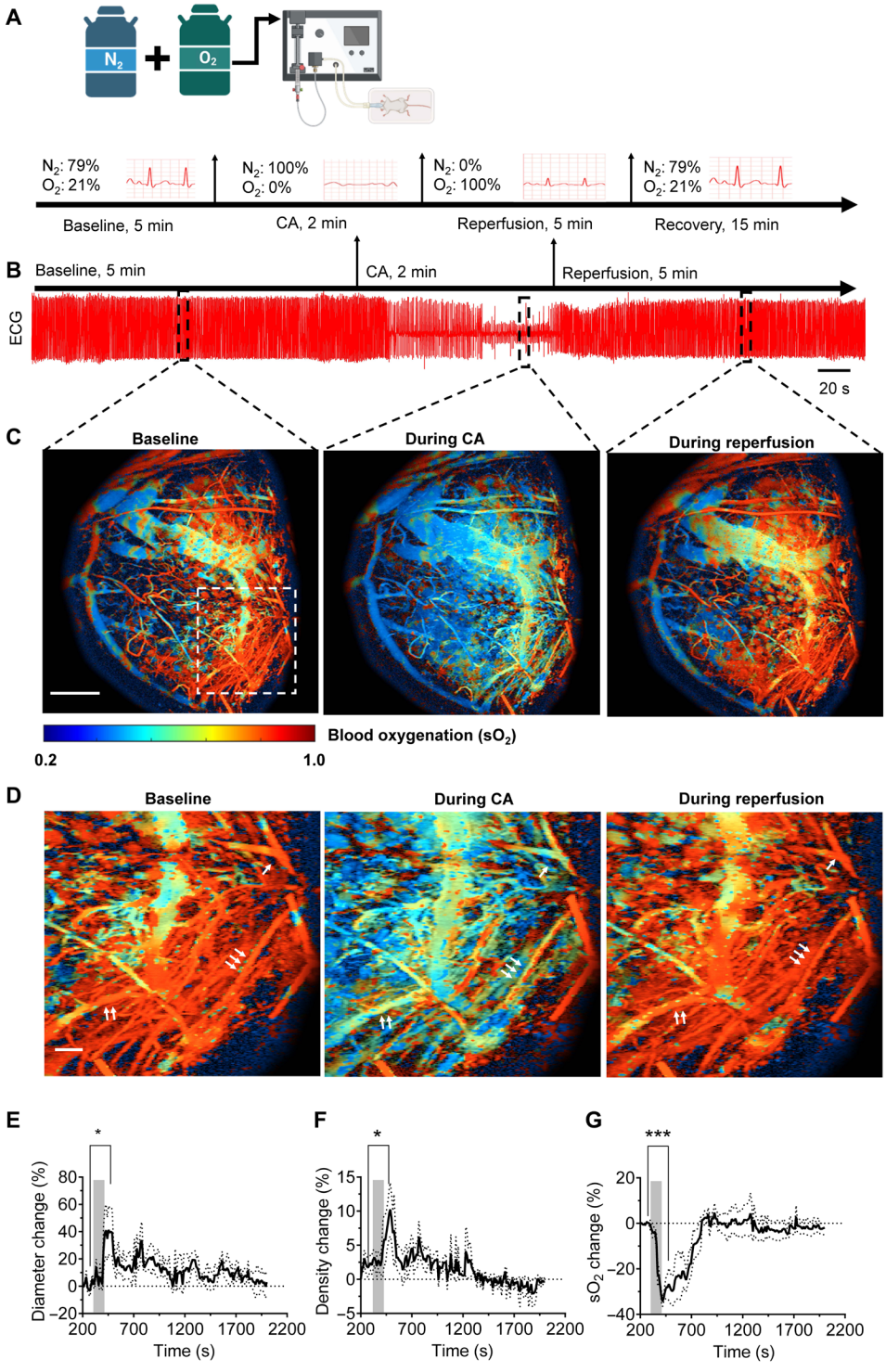

Fig. 5. Rapid placental responses to CA. (**A**) Experimental setup of the CA challenge. The animal was under normoxia for 5 min with 21% O_2, CA for 2 min with 100% N_2, reperfusion for 5 min with 100% O_2, and then 15 min recovery with 21% O_2. UFF-PAM was performed throughout the experiment. (**B**) Continuous ECG recording of the mouse before, during, and after the CA challenge. The heart beating rate dropped from 73 to 0.25 Hz during the CA. (**C**) Snapshot UFF-PAM sO_2 images of the mouse placenta during baseline at 50 s, CA challenge at 350 s, and reperfusion at 700 s. There was clear placental hypoxia induced by CA. Scale bar, 1 mm. (**D**) Close-up images of the region indicated by the white dashed box in (C), showing the detailed vascular response during the CA challenge and the reperfusion. Scale bar, 200 μm. (**E**) The averaged vessel diameter change shows CA-induced vasodilation, mostly due to the elevated CO_2 level in the blood. The gray box represents the duration of 100% N_2 treatment. (**F**) The vessel density had a moderate increase, due to a combined outcome of reduced blood perfusion and increased vessel diameters. (**G**) Substantial decrease in the blood oxygenation was induced by the CA challenge due to the lack of perfusion. $N = 3$ mice. The data are shown as mean ± SEM. *$P < 0.05$; ***$P < 0.001$.

Inflammation and placental hemodynamics

Placenta not only provides oxygen and nutrients to the fetus but also protects the fetus from immune-mediated impairments. The maternal-fetal interface has unique immune characteristics to protect the semi-allogeneic fetus from rejection by the maternal immune system. Disruption of the fine-tuned immune balance in the placenta has been linked with multiple pregnancy complications. For example, lipopolysaccharide (LPS)–induced inflammation can compromise the development of the placenta and lead to preterm birth or PE, which are leading causes of maternal and fetal morbidity and mortality (*64*). Using UFF-PAM, we examined the longitudinal hemodynamic changes from E7.0 to E13.0 induced by systemic LPS administration starting from E8.0 (Fig. 6A). The treated mice were terminated at E13.0 before the potential preterm labor. The longitudinal PA images showed that the LPS-treated mice had distinct placenta vasculature compared with the control mice treated with saline (Fig. 6, B to D, and movie S8). The microvessel density of the LPS-treated placenta was substantially lower than the control group, while the major vessel diameters were increased. Quantitatively data analysis showed that the averaged vessel diameter of the LPS-treated placenta was >100% lower (Fig. 6E), and the vessel density was >70% lower than that of the control group at E11.0 to E13.0 (Fig. 6F), both of which might be due to the impairment of microvessel development in the LPS-treated group. The averaged sO_2 level of the LPS-treated placenta from E9.0 to E11.0 was substantially higher than that of the control group (Fig. 6G). Normally, the placenta should be hypoxia at this stage of its development as described in Fig. 3D. Apparently, LPS treatment disrupted the low-oxygen environment (or hypoxia) that promotes angiogenesis and protects the developing placenta and fetus from oxidative stress. This observation is concordant with the impeded microvessel development manifested by the reduced vessel density in pervious findings by us and others (*65*–*67*).

Tracking placenta viral transduction and chemical diffusion

Monitoring the mobility of molecules within the placenta carries substantial scientific significance (*5*). It can provide valuable insights into the transport and regulation of vital substances in the placenta, such as nutrients and virus, in both healthy pregnancy and pregnancy pathologies (*68*–*71*). It can also enhance our understanding of how drugs or therapeutic molecules traverse the placental barrier, offering insights for the development of safe and effective treatments of pregnancy diseases (*72*). Adeno-associated viruses (AAVs) are used extensively as delivery vehicles for in vivo gene delivery and clinical gene therapy applications (*73*, *74*). We had previously showed the transduction process of AAV vectors into the embryos by using the intravital embryonic window and fluorescence imaging (*24*). Here, we placed an intravital placenta window in pregnant mice on E7.0 and injected AAV serotypes 8 carrying a green fluorescent protein (GFP) reporter into the orbital veins of dams at E8.5 (Fig. 7A). Two-photon microscopy was then performed to continuously image the placentas at the single-cell level, 72 hours after the AAV injection (Fig. 7B). Via the placenta window, we clearly observed volumetric GFP expression in the placentas at E11.5 with single-cell resolution and depth sectioning (Fig. 7C and movie S9). Using the vasculature on the surface of the uterus and in the placenta as a reference roadmap (fig. S8), we traced the GFP-expressing cells in the same region for up to 48 hours (Fig. 7C and fig. S9A). Our imaging showed that AAV vectors can be used to deliver genes into the placenta, which might be used to study the specific gene functions during placental development.

Moreover, the placenta serves as a barrier that impedes chemicals such as drugs or fluorescent markers from entering the embryo (*75*). We had tested passage of fluorescein through the umbilical cord and its subsequent diffusion into the embryo (*24*). Here, using wide-field fluorescence microscopy, we have observed the diffusion process of fluorescein into the placenta via an intravital placenta window installed on E7.0 (Fig. 7D). In 10 s after injection of fluorescein through the dams' orbital vein on E8.5, we observed its fast diffusion into the placenta vasculature, subsequentially the whole placenta in 5 min after injection (Fig. 7E, fig. S9B, and movie S10). Taking advantage of the high imaging speed, we observed that the placental arteries were first perfused with fluorescein by 15 s after injection, as validated by the UFF-PAM image acquired later (Fig. 7F). The results have demonstrated that fluorescent probes (e.g., AAVs and labeled drugs) can be used to track the molecular transportation inside the placenta via the placenta window.

DISCUSSION

Abnormalities in placental functions can cause several deadly pregnancy pathologies, including PE, restricted fetus growth, and preterm birth. Since there are no effective therapies for these pregnancy diseases, small animal models are necessary to investigate causal pathways, develop new preventive measures and therapies, and evaluate their safety and efficacy. Current placental studies mostly rely on ex vivo placental tissues, which do not provide adequate information on the dynamic placental development. In vivo imaging of the placental functions is pressingly needed for solving this problem. However, in vivo imaging of placental development has been challenging due to its depth in the abdominal cavity and severe motion. To overcome these hurdles, we have developed an intravital imaging platform that can safely monitor placental development throughout pregnancy, thereby improving our understanding of placenta hemodynamics and molecular activities in small animal models.

To address the depth issue, we have developed and optimized the first implantable placenta window with the accompanying microsurgical procedure. This is not a trivial task as the placenta is extremely sensitive to the environment such as stress, perfusion, and temperature. Our intravital window technique provides direct access to the placenta for continuous imaging starting as early as E7.0. The window is both optically and acoustically transparent, making it ideal for high-resolution photoacoustic and fluorescence imaging. In addition to photoacoustic imaging, the placenta window can be used for other optical imaging methods as well, which is more widely available for placenta researchers. For example, we used two-photon microscopy to keep track of the GFP expression after AAV transduction. We also used wide-field fluorescence microscopy to track the diffusion of fluorescein into the placentas. The placenta window did not affect the fetus's organ formation, delivery, or feeding. However, we observed that embryos under the window had relatively low weight, possibly due to heat loss, which is known to contribute to intrauterine growth restriction (*76*). The weight reduction under the window can also be attributed to several other possible factors, including the restriction of placental blood flow due to pressure from the window and the coiling or twisting of the

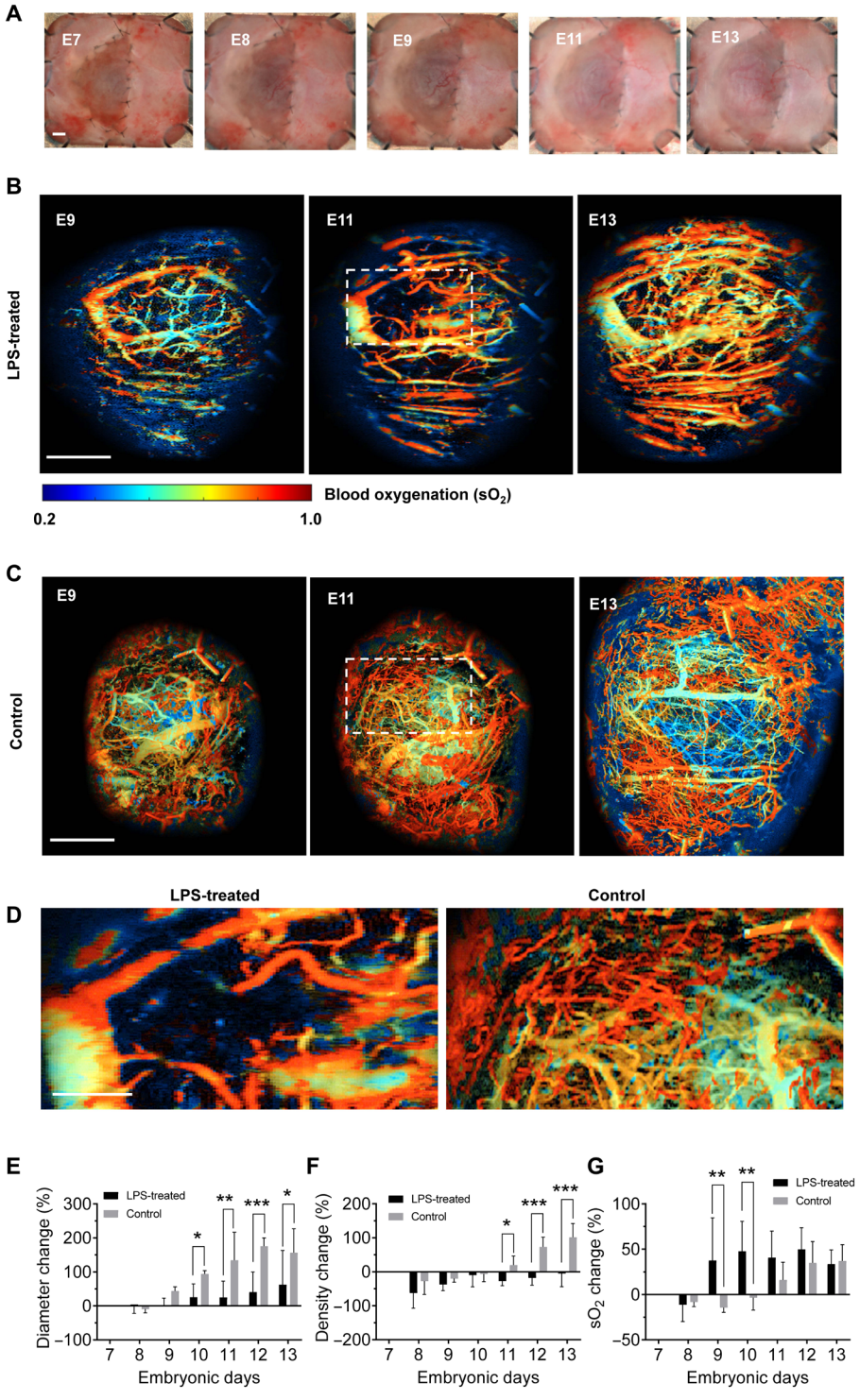

Fig. 6. Longitudinal monitoring of placentation in the LPS-induced inflammation model. (**A**) Photos of the pregnant mouse from E7.0 to E13.0, with the window installed on E7.0. The pregnant mice were treated with LPS (0.5 mg/kg) at E8.5 once to induce inflammation. Scale bar, 1 mm. (**B**) Representative UFF-PAM sO_2 images of the LPS-treated mouse placenta from E7.0 to E13.0, showing a lack of microvessels. Scale bar, 1 mm. (**C**) Representative UFF-PAM sO_2 images of the control mouse treated with saline, showing the dense microvessels and normal major vessels. (**D**) Close-up images of the region indicated by the white dashed box in (B) and (C), showing the reduced microvessel density in the LPS-treated placenta. Scale bar, 200 μm. (**E**) Vessel diameter change from E7.0 to E13.0, showing that the LPS-treated placenta had less change in the vessel diameter, mainly due to the lack of microvessels. (**F**) Vessel density change from E7.0 to E13.0, showing that the LPS-treated placenta had much less new vessels developed. (**G**) Blood oxygenation change from E7.0 to E13.0, showing that the LPS-treated placenta had much higher oxygenation at the early stage. $N = 3$ mice. The data are shown as mean ± SEM. *$P < 0.05$; **$P < 0.01$; ***$P < 0.001$.

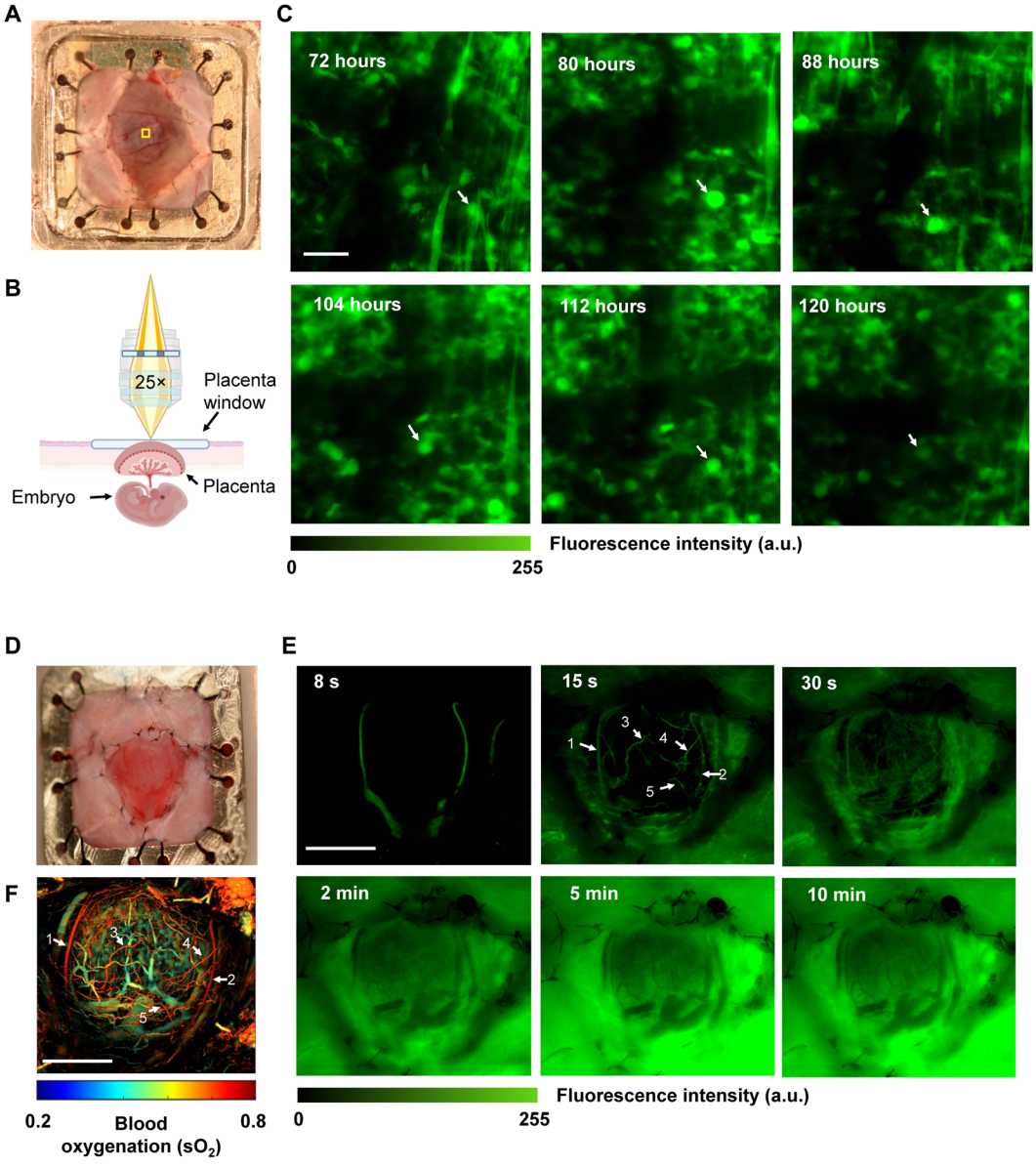

Fig. 7. Tracking viral transduction and chemical diffusion via the placenta window. (**A**) Photo of a placenta that was imaged through the placenta window implanted on E7.0. GFP-AAVs were injected on E8.5. (**B**) Two-photon microscopy was performed to track the GFP expression in the placenta over 48 hours after AAV transduction. The field of view is indicated by the yellow rectangle box of (A). (**C**) Representative two-photon microscopy images of the GFP-expressing cells in the placenta over 48 hours, showing the progressive cell transduction with single-cell resolution. The arrows point to the trace of representative GFP-expressing cells over 48 hours. Scale bar, 100 μm. $N = 3$ mice. (**D**) Photo of a placenta on E11.5 with the window implanted on E7.0. Fluorescein was injected via the orbital vein, and the fluorescein diffusion into the placenta was tracked using wide-field fluorescence microscopy. (**E**) Fluorescence images of the placenta started several seconds after the fluorescein injection, and the fluorescein diffusion into the entire placenta took around 30 min. The fluorescein first diffused into the placental arteries, as indicated by the arrows in the image at 15 s. Scale bar, 2 mm. $N = 3$ mice. (**F**) UFF-PAM sO_2 image of the same placenta, confirming the fluorescein-perfused arteries identified by the fluorescence imaging in (E). Scale bar, 2 mm. a.u., arbitrary units.

placental artery. To address this issue, the placenta window can be improved by adding a heating circuit with temperature feedback to the window cap. More work is needed to better understand the window's impact on the pregnancy and further improve the window's biocompatibility.

Second, to address the issue of motion artifacts, we have further upgraded our UFF-PAM, which is capable of high-speed, wide-field, high-resolution imaging of the placenta in vivo. UFF-PAM can provide functional imaging of the placental blood oxygenation without the need of an exogenous contrast agent, which is not available for other imaging modalities. Two generations of UFF-PAM have been applied in our studies: The first-generation system used a post-objective scanning strategy, and the upgraded second-generation system used a pre-objective scanning strategy. Both systems can provide a large field of view (1 cm^2) and motion-free images of the placental hemodynamics. Compared with the first-generation

system, the second-generation system has improved stability and 10-fold higher maximum imaging speed but 3-fold lower detection sensitivity. As of now, both UFF-PAM systems represent the fastest PAM technology.

Combining the intravital placenta window and the state-of-the-art UFF-PAM, we were able to study the developing mouse placenta under healthy and pathological conditions. Our UFF-PAM images have provided the first experimental evidence of placental hemodynamics with microvessel-level details that were not known before. For healthy pregnancy, our results showed an increase of the sO_2 level until E15.0 and then a decrease until birth. The hypoxic condition at the beginning of the first trimester is believed to be beneficial for reducing the oxidative stress on the early-stage embryo and promoting the trophoblast invasion of the maternal spiral arteries. The oxygenation gradually improves during the first trimester likely because of the increased oxygen consumption from the formation of the placenta to the organogenesis of the embryo. The decrease in oxygenation during the second semester might be for the preparation of delivery. Under the challenge of chronic alcohol consumption, previous reports have shown increased placental blood perfusion but with limited imaging resolution and speed (*53*). Our UFF-PAM allowed for observing the real-time hemodynamic changes of the placenta immediately after alcohol consumption in otherwise healthy pregnant mice. Our results showed a rapid increase in placental blood perfusion and oxygenation induced by alcohol, particularly on the microvessels, which might have an adverse impact on the fetus due to elevated oxidative stress. The long-term impact of alcohol exposure on placenta health remains to be studied.

We have also investigated the impact on placental hemodynamics by two deadly disease models: CA and inflammation. CA in pregnant women is one of the most challenging clinical obstetric emergencies. There is very limited knowledge of placental hemodynamics during CA. Our UFF-PAM results have documented rapid vasodilation, reduced blood perfusion, and decreased oxygenation induced by CA, resulting in prolonged hypoxic conditions in the placenta even after heart resuscitation. Inflammation is a common pregnancy complication. LPS can induce inflammation-like phenotype in mouse models. Our UFF-PAM results have confirmed a declined chorionic structure on the LPS-induced inflammation model. We have experimentally confirmed a drastic decrease in the microvessel density after LPS administration, which has not been imaged before. Since microvessels are the primary regulator of blood flow and oxygen delivery, our results have strongly suggested the reduced density of microvessels might be a causal factor rather than a consequence of inflammation.

We would like to acknowledge that all the in vivo studies demonstrated in our work led to systematic responses in the placenta hemodynamics. Thus, we only chose a small number of representative blood vessels for detailed analysis. For future studies in which we expect region-specific responses, more sophisticated vessel segmentation methods can be applied to automatically analyze individual vessels within different regions over the entire field of view. In the future work, it is also necessary to apply the placenta window on other animal species with relatively long pregnancy, such as rats (~23 days pregnancy) and rabbits (~31 days pregnancy), which may reduce the wound healing complications during pregnancy. We will also explore the immunohistochemical staining to further study any abnormality in the placental tissue beneath the window. For example, we can perform monocarboxylate transporter 1 and 4 immunofluorescence staining of the placentas to exam any blood vessel deficiency of both maternal and fetal vasculature.

In summary, we have developed an intravital placenta imaging technology that combines a transparent placenta window and high-speed high-resolution imaging methods. Through proof-of-concept studies, we have presented solid evidence of the capability of our intravital imaging platform to study the placental hemodynamics and molecular activities of small animal models in vivo. Our imaging technology has achieved longitudinal monitoring of placental development throughout healthy pregnancy and investigated imaging biomarkers of placental pathology, including the vasculature morphology, hemodynamic functions, and gene expression. We believe that this placenta window technology can be readily expanded to many other imaging modalities and applied to the broad placenta research and reproductive medicine. We expect that our technology can provide important knowledge on placenta biology, as well as clinical insight on managing pregnancy-related diseases, such as placenta accreta, preterm birth, fetal brain damage, as well alcohol and opioid abuse.

MATERIALS AND METHODS

Animal preparation

All animal procedures were reviewed and approved by the Institutional Animal Care and Use Committee of Duke University (protocol nos. A139-18-05 2018-2021 and A088-21-05 2021-2022) and were conducted in accordance with National Institutes of Health guidelines. CD1 mice (10 to 16 weeks old; weight, 25 to 35 g) were obtained from Charles River Laboratories and applied in all the experiments. Mice were maintained in a specific pathogen–free environment with a fixed 12-hour/12-hour light/dark cycle, and food and water were available at Division of Laboratory Animal Resources. Mating was performed overnight, and noon on the day of plug detection was considered E0.5. During imaging experiments, the mice were under anesthesia with 1.5% (v/v) isoflurane, and the body temperature was maintained at 37°C using a heating pad.

Standard $N = 3$ independent experiments were performed for most cases, unless noted in the figure legend. With proof-of-concept studies, we minimized the number of animals to achieve the scientific objectives, conferring to the requirements of the Association for Assessment and Accreditation of Laboratory Animal Care International standards for the humane care and use of animals (https://aaalac.org/the-guide/). Group allocation used in our study was randomly assigned to animals. Blinding was not relevant to our studies because we often evaluated the same animals responding to the physiological challenges. No data were excluded.

Fabrication of the placenta window and clip

The window frames, stainless-steel covers, and clip were designed using SOLIDWORKS 2020. The window frames and covers were made of titanium by precision machining in Duke Physics Store. The clip to stabilize the window was printed by an Ultimaker 2+ 3D printer with polylactic acid filament.

Surgical procedure for implanting the placenta window

The surgeries were conducted by a proficient surgeon Q. Huang in a meticulously sterile environment. Before the window implantation, all surgical instruments were properly sterilized. Pregnant mice were

anesthetized using 2% (v/v) isoflurane with oxygen at 2 liters/min. The abdomen was depilated appropriately and cleaned with 70% ethanol and iodine. After covering it with a sterile field, a square incision was made in the abdomen, removing some of the skin. Two incisions were made in the abdominal muscle, one was a midline incision and the other one was a midclavicular line incision. One side of the uterus was taken out from the abdominal cavity, and the placenta side was exposed. The downside of the placenta was sutured to the midline incision, and the upside of the placenta was sutured to the far edge of the midclavicular line incision. The IWF was sutured with the abdominal muscle appropriately using inverse mattress suture. To avoid the blocking of blood flow because of the mechanical pressure, we left enough space between the IWF and the placenta and filled the space with Matrigel. A piece of optically and acoustically transparent membrane was attached to the OWF using ultraviolet glue. Then, the OWF was attached to the IWF using dental screws. The incision was closed by attaching the OWF to the skin using surgical glue. Then, we secured the window cap on the top of the OWF with screws. All the placenta windows were implanted at E7.0.

Because of the pregnancy, there are several factors that could affect the healing after the window implantation, such as pain, inflammation, maternal stress, and hormone changes. To alleviate pain and inflammation, all animals undergoing surgery were anesthetized with isoflurane, and pain killers were used before and after the surgical procedure. Specifically, we used bupivacaine as a local analgesic before surgery, and we supplied meloxicam, a nonsteroidal anti-inflammatory drug, for 3 days following surgery. To alleviate discomfort during anesthetized procedures, such as surgery, we used ophthalmic eye ointment to prevent drying of the eyes during anesthesia. Mice were housed individually postoperatively to prevent infection at surgical sites and damage to the implant; in these scenarios, the mice were provided with enrichment objects to limit discomfort and distress associated with isolation. Following all procedures, we monitored animal well-being, such as body weight, grooming tendencies, surgical site infection, signs of pain or distress, self-mutilation, neurological disorders, cardiopulmonary disorders, abnormal feeding or defecation, and nonweight bearing posture, as indicators for mouse discomfort. For all the surgeries performed in this study, we did not observe clear wound healing complications on the dams.

Ultrafast functional PAM

PAM is a hybrid in vivo imaging technique that detects ultrasound signals induced by optical absorption. Light absorbed by molecules in tissue is partially or completely converted into heat, the heat-induced pressure rise propagates as ultrasound waves and is detected by ultrasound transducer(s) to form images. Compared to the pure optical microscopic techniques, PAM takes advantage of the weak acoustic scattering in tissue and thus can penetrate deeper. Besides, PAM provides endogenous absorption contrasts of hemodynamics using hemoglobin as the contrast (*26, 77–79*). In this work, we used two generations of UFF-PAM to study the hemodynamics of placenta development: (i) the Gen1-UFF-PAM system with post-objective scanning and spherically focused ultrasound transducer (*30*), to monitor blood vessel development continuously (6 s per volumetric frame rate); (ii) the Gen2-UFF-PAM system with pre-objective scanning and cylindrically focused ultrasound transducer, to track fast dynamic changes under physiological stimulation in real-time (0.5 s per volumetric frame rate).

The laser source and Raman path

To capture the vascular structure and the oxygenation map simultaneously, we used two lasers to provide dual-wavelength PA excitation. Both lasers generate a 532-nm pulsed light beam. The first laser (VPFL-G-20, Spectra-Physics) was used to provide 532-nm light, and the other laser (SPFL-532-40, Spectra-Physics) was used to pump a Raman shifter to generate 558-nm light. The maximum pulse repetition rate used in our study was ~800 kHz. In the Raman path, the laser polarization state was adjusted by a half-wave plate (AHWP05M-580, Thorlabs) to achieve a high Raman shift efficiency. The 532-nm pump beam was focused by an objective (UPLFLN 20×, Olympus) into a 6.5-m polarization-maintaining single-mode fiber (HB450-SC, Fibercore). To achieve a high coupling efficiency, the fiber was mounted on a fiber alignment stage (561D-XYZ, Newport) connected with a bare fiber chuck (FPH-S, Newport) for precise and robust alignment. A universal bare fiber terminator (BFT1, Thorlabs) was used to fix the fiber tip and avoid thermal or air disturbance. An achromatic fiber port (PAF2A-A10A, Thorlabs) was used to collimate the output beam. The maximum Raman shifting frequency of the single-mode fiber was ~13.2 THz, corresponding to the first stroke at 545 nm and the second stroke at 558 nm. We chose the second stroke at 558 nm for better contrast between the oxy- and deoxy-hemoglobin. A dichroic mirror (DMSP550, Thorlabs) was used to filter out the 532-nm and the 545-nm light. The conversation efficiency for 558-nm light was about 33%. The 532-nm light beam and the 558-nm light beam were combined by a dichroic mirror (DMSP550, Thorlabs). The laser pulse pair at 532 and 558 nm was fired with a time interval of 300 ns. sO_2 was quantified by calculating the relative concentrations of oxy-hemoglobin from the detected dual-wavelength PA signals. A flip mirror was used to switch the combined laser beams between two UFF-PAM systems detailed below.

First-generation UFF-PAM

This system has been used for real-time whole-brain imaging of hemodynamics and oxygenation at microvessel resolution and demonstrated a great potential for fundamental research under various pathological and physiological conditions (*30*). In this research, we optimized the imaging parameters and applied it for continuously monitoring hemodynamic development in the placentas. In this system, the combined laser beam was focused by an objective lens (AC127-050-A, Thorlabs) and passed through the central aperture of a spherically focused ring-shaped ultrasound transducer (central frequency, 40 MHz; bandwidth, 100%; focal length, 14 mm). A 12-facet polygon scanner was positioned close to the front surface of the transducer. Driven by a water-immersible high-speed DC motor, the polygon scanner steered both the combined laser beam and the resultant ultrasound wave simultaneously. The system can achieve a maximum B-scan rate of 2 kHz along the fast-scanning axis over a 10-mm scanning range, which was sufficient to cover the entire placenta window. The scanning speed was adjusted by changing the driving current of the DC motor. To capture the detailed placenta blood vessels, we reduced the B-scan rate to 0.5 kHz to increase the spatial sampling density (i.e., smaller step size) and improve the image quality. We used a motorized stepper motor along the slow axis for volumetric imaging. In the placenta imaging, we usually acquired a volumetric image over a field of view of 11 mm × 7.5 mm × 1.5 mm, which took 6 s. Fast scanning speed was crucial for precisely capturing the vascular structure and the vessel-by-vessel oxygenation map since the uterine peristalsis and respiration

motion could cause severe motion artifacts. The focused laser spot on the placenta ranged from 7 to 18 μm along the fast axis, with a smaller spot in the middle and a larger spot on the edges. Thus, the spatial resolution and ultrasound detection sensitivity were not uniform along the fast axis scanning.

Second-generation UFF-PAM

We also developed the Gen2-UFF-PAM which achieved higher imaging speed and better scanning stability and uniformity at high speeds. Instead of using the water-immersible polygon scanner as in the Gen1-UFF-PAM, the combined laser beam was scanned by a 16-facet polygon scanner (GECKO-45-HSS, Precision Laser Scanning) rotating in the air which was more stable than the water-immersible polygon scanner. We designed the light path based on the optical invariant analysis (*80*). Steered by the polygon scanner, the laser beam was relayed to the rear aperture of an objective (AC254-040-A, Thorlabs) with two lens systems (AC254-030-A and AC254–100-A, Thorlabs). The optical invariant of the objective was equal to the invariant at the polygon scanner. Then, the combined laser beam passed through the rectangular opening of a cylindrically focused ultrasound transducer (central frequency, 40 MHz; bandwidth, 100%; focal length, 7 mm). To maximize the detection sensitivity, the laser beam was scanning along the acoustic focal lane of the cylindrical transducer. The optical beam spot size on the sample surface was ~5 μm, consistent across the scanning range. The maximum line scanning rate of the polygon scanner was 12 kHz. To maintain the image quality, we chose a 2-kHz line scanning rate along the fast axis. A stepper motor scanned along the slow axis. Each B-scan over a 9-mm range was sufficient to cover most of the entire placenta window. Each volumetric image took 0.5 s, which was 12 times faster than the Gen1-UFF-PAM.

Cylindrically focused ultrasound transducer

As shown in fig. S4, a 40-MHz cylindrical ultrasound transducer was customized for 1D focusing in the Gen2-UFF-PAM. A rectangular opening was used for the laser beam to pass through. High-speed line scanning along the acoustic focal line was realized. First, lithium niobate (LNO) (Boston Piezo-Optics, Bellingham, MA, USA) was chosen as the core piezoelectric material for acoustic-electrical conversion due to the strong piezoelectric effect and low permittivity, which is suitable for electrical impedance matching (~50 ohms) of transducers with large aperture sizes. On the basis of the material parameters, a piezoelectric transducer modeling software (PiezoCAD), based on Krimboltz, Leedom, and Mattaei equivalent circuit model, was used to optimize the design of the transducer with a 10-mm length, 6-mm width, 70-μm thickness, and a 2-mm-wide opening in the center. Then, the customized LNO plate was lapped down to the thickness of 70 μm for a 40-MHz piezoelectric element. A Cr/Au (50/100 nm) electrode was sputtered on both sides of the lapped LNO plate. Next, the first matching layer (a mixture made of 2- to 3-μm silver powder loaded epoxy, acoustic impedance ~7.3 MRayl) and backing material (a commercial conductive silver paste, E-solder 3022, Von Roll Isola, acoustic impedance ~5.9 MRayl) were deposited onto the corresponding sides of the plate. After curing, the first matching layer and backing material were lapped down to 10 μm and 3 mm, respectively. The matched and backed acoustic stack was mechanically cut into smaller pieces with a length of 10 mm and a width of 6 mm. Then, the acoustic stack was fixed in an aluminum house. The gap was filled with epoxy resin (EPO-TEK 301, Epoxy Technology), and one lead wire was connected through the backing. The transducer was then hot pressed in an oven at 90°C by a metal cylinder to form a focal length of 7 mm. After that, mechanical cutting was used for the 2-mm opening formation to let the laser pass. Another Cr/Au (50/100 nm) electrode was sputtered across the first matching layer and the brass housing to form a common ground connection. Last, a 10-μm-thick Parylene-C film was deposited onto the entire external surface of the transducer as the protective layer and the second matching layer. The two matching layers with a thickness of a quarter wavelength can compensate for the acoustic impedance mismatch between the LNO piezoelectric plates (~34.5 MRayl) and the biological tissues (~1.5 MRayl).

Start-of-scan detection

Polygon scanners are designed to run at a constant speed, with each facet steering the laser beam over the same scanning trajectory. By detecting the start of the line scan by each facet, we can know the positions of the steered laser beam throughout the scan. As the rotation of the polygon is independent of the laser firing, we built a start-of-scan (SOS) system by detecting the PA excitation light using a multimode optical fiber (M45L02, Thorlabs) positioned at the start of the scanning trajectory. A photodiode (PDA36A2, Thorlabs) received the SOS light and converted it to an electrical trigger that can be used to synchronize the data acquisition and slow axis scanning. In the Gen1-UFF-PAM, the multimode fiber was immersed in the water beneath the spherical ultrasound transducer. In the Gen2-UFF-PAM, the multimode fiber was positioned in the air right after the polygon scanner.

Data acquisition and data analysis

The PA signals with dual-wavelength excitation were first amplified and low-pass–filtered (BLP-50+, Mini-Circuits) and then sampled by a data acquisition card (ATS9350, AlarzarTech) with a 250-MHz sampling rate. No signal averaging was applied. The acquired data were then analyzed using MATLAB.

Intraperitoneal injection of alcohol

Pregnant mice at E12.5 were used for this experiment. After baseline imaging for 2 min, ethanol (3.0 g/kg; Sigma-Aldrich, catalog no. E7023) was injected into the abdominal cavity via intraperitoneal injection. The resultant physiological changes of the placentas were continuously imaged by UFF-PAM for 10 min.

CA induction and imaging

Pregnant mice at E12.5 were used for this experiment. CA was induced by increasing the nitrogen content of the respiratory air from 79 to 100%. The heart beating rate was monitored by an ECG recorder. After baseline imaging for 5 min, we introduced nitrogen for 2 min and imaged the resultant physiological changes in the placenta. The change in ECG before CA was due to the delay in the CA induction using 100% nitrogen. After the nitrogen induction, we applied 100% oxygen for 5 min and then monitored the mice continuously for another 15 min.

LPS-induced inflammation

The pregnant mice were treated with LPS (0.5 mg/kg; Sigma-Aldrich, catalog no. L7895) at E8.5 once. The physiological changes of placentas were imaged by UFF-PAM for 5 min every day from E7.0 to E13.0. The mice were terminated at E13.0 due to the worsening pathological conditions.

AAV production

Human embryonic kidney 293 cells were grown in Dulbecco's modified Eagle's medium, supplemented with 10% fetal bovine serum (Sigma-Aldrich) and 1% penicillin-streptomycin (Thermo Fisher Scientific) at 37°C in an 5% CO_2 incubator. A triple plasmid transfection method was used to produce recombinant AAV vectors: an AAV plasmid (pXR8g9, encoding AAV2 replication proteins), an adenoviral helper plasmid (pXX680), and a transgene packaging cassette, encoding self-complementary GFP driven by a chicken β-actin hybrid promoter (pTR-CBh-scGFP), flanked by AAV2 inverted terminal repeat (ITR) sequences. The purification of viral vectors was through iodixanol density gradient ultracentrifugation, subjected to phosphate-buffered saline (PBS) buffer exchange using Zeba Spin 40-kDa molecular weight cutoff desalting columns (Thermo Fisher Scientific, 87772). Quantitative polymerase chain reaction was used to detect the titers of purified virus preparations by amplifying the AAV2 ITR regions (forward, 5′-AACA TGCTACGCAGAGAGGGAGTGG-3′ ;reverse, 5′-CATGAGAC AAGGAACCCCTAGTG ATGGAG-3′) (Integrated DNA Technologies, Ames, IA).

Orbital vein injection of AAV and fluorescein

Fluorescein (10 mg/kg; Sigma-Aldrich, catalog no. F2456) was injected through the orbital vein at E11.5. AAVs (1×10^{11}) were injected via the orbital vein at E8.5.

Two-photon microscopy

Mice were placed on an imaging stage, stabilized by 3D-printed clips with eye ointment, and anesthetized with isoflurane. In vivo imaging to track the single-cell labeled with AAV was performed using a Leica SP8 two-photon DIVE, 72 hours after the AAV injection. The enhanced GFP (eGFP) excitation wavelength was 920 nm. A 25×/1.05 numerical aperture water immersion objective with a motorized correction collar was used to image the eGFP-labeled cells.

Stereoscope fluorescence microscope imaging

Mice were anesthetized and placed on the imaging stage. A Zeiss Lumar.V12 stereoscope was used to image the whole placenta. Fluorescence emission was collected at 515 to 565 nm for the detection of eGFP signals.

Hematoxylin and eosin staining

After the completion of PAM imaging sessions, the fetuses and placentae were isolated by mechanical dissection of the conceptus at E18.5, and their wet weights and morphology were recorded immediately after collection. Then, the embryos and placentas were fixed in the 4% paraformaldehyde in PBS for 72 hours. The embryos were sacrificed with decapitation, and some of the skin was removed for sufficient fixation. Then, the samples were put into 70% ethanol and embedded in paraffin after dehydration. The sections were cut at 5-μm thickness for hematoxylin and eosin staining. For deparaffinization and rehydration, the sections were sequentially treated with xylene (2 min × 2), 100% ethanol (2 min × 1), 95% ethanol (2 min × 1), 80% ethanol (2 min × 1), 70% ethanol (2 min × 1), and distilled water (3 min × 2). The slides were immersed in hematoxylin and eosin solution for 2 min each. After dehydration with 95% ethanol (2 min × 1) and 100% ethanol (2 min × 1), the slides were mounted for further observation.

Blood collection and whole blood component test

Blood (0.5 ml) was collected by the cardiac puncture after the dams were euthanized with 3% (v/v) CO_2. A total of 0.1 ml of blood from each embryo was collected by the decapitation. The whole blood components were analyzed by the Hemavet veterinary hematology analyzer.

Statistical analysis

We conducted quantitative data analyses based on the imaging results to examine vasculature development and hemodynamic changes in the placenta throughout mouse pregnancy under normal and pathological conditions. These pathological conditions included acute physiological challenges such as alcohol consumption and CA, as well as chronic hemodynamic abnormalities in a mouse PE model.

To extract the vessels from the background, we used a lab-developed segmentation method, as previously published (*27*, *43*). Briefly, before quantitative analysis, the photoacoustic signal amplitude in each image was extracted through a Hilbert transformation of the recorded data, and vessel segmentation was performed using a MATLAB Image Processing Toolbox (R2019b, MathWorks, Boston, MA). As shown in fig. S7, the first step is to separate the vessel pixels from the background pixels. Here, we used three times the SD of the background signals as the threshold. The background pixels were then set to zero. The second step is to identify and isolate each single vessel from the vasculature network using vessel segmentation. Each vessel was identified and labeled by tracking its axis in 3D space. The daughter vessels branching from the mother vessel were labeled as different vessels. The third step is to characterize individual vessels such as the vessel diameter and the total pixel number of vessels. The vessel diameter was measured as the shortest distance across the vessel lumen, i.e., the full width of the vessel. The vessel density was measured as the ratio of vasculature area to total field of view. The vasculature area was counted to include all segmented vessels. To analyze the sO_2, we used a well-established linear signal unmixing technique to calculate the relative concentrations of HbR and HbO_2 from the two photoacoustic images acquired at 532 and 558 nm (*28*). The average sO_2 was calculated over all the blood vessels in the field of view, including both arteries and veins.

We measured the average vessel diameter, vessel density, and average sO_2 (including both arteries from veins). We analyzed a total of six to eight arteries and six to eight veins per placenta, with vessels selected randomly. In case of longitudinal or continuous observation, we consistently selected the same set of blood vessels for diameter measurements. When capturing dynamics to observe placental acute responses, we chose the same vessel positions to measure the same blood vessels during the acute responses. These vessels were then subjected to detailed analysis. Hemodynamic parameters were quantified across the entire field of view. For multiday monitoring, the quantifications at different time points were compared with the baseline to minimize the inter-animal variation, and the relative percentage changes were reported. We used paired *t* tests for all analyses and presented the statistical data with the SEM. A *P* value of <0.05 was considered significant.

In addition, to compare the parameters between embryos or mice with and without the placenta window, we used Student's *t* test. Statistical analysis was performed using the SPSS 18.0 statistical package.

Supplementary Materials

This PDF file includes:
Figs. S1 to S9
Table S1
Legends for movies S1 to S10

Other Supplementary Material for this manuscript includes the following:
Movies S1 to S10

REFERENCES AND NOTES

1. A. G. Campbell, G. S. Dawes, A. P. Fishman, A. I. Hyman, G. B. James, The oxygen consumption of the placenta and foetal membranes in the sheep. *J. Physiol.* **182**, 439–464 (1966).
2. D. R. Bonds, L. O. Crosby, T. G. Cheek, M. Hagerdal, B. B. Gutsche, S. G. Gabbe, Estimation of human fetal-placental unit metabolic rate by application of the Bohr principle. *J. Dev. Physiol.* **8**, 49–54 (1986).
3. R. C. Vandenbosche, J. T. Kirchner, Intrauterine growth retardation. *Am. Fam. Physician* **58**, 1384–1390, 1393–1394 (1998).
4. L. D. Wang, K. Maslov, J. J. Yao, B. Rao, L. H. V. Wang, Fast voice-coil scanning optical-resolution photoacoustic microscopy. *Opt. Lett.* **36**, 139–141 (2011).
5. M. Dilworth, C. Sibley, Review: Transport across the placenta of mice and women. *Placenta* **34**, S34–S39 (2013).
6. N. A. Portilho, M. Pelajo-Machado, Mechanism of hematopoiesis and vasculogenesis in mouse placenta. *Placenta* **69**, 140–145 (2018).
7. K. L. Gatford, P. H. Andraweera, C. T. Roberts, A. S. Care, Animal models of preeclampsia: Causes, consequences, and interventions. *Hypertension* **75**, 1363–1381 (2020).
8. M. Hemberger, C. W. Hanna, W. Dean, Mechanisms of early placental development in mouse and humans. *Nat. Rev. Genet.* **21**, 27–43 (2020).
9. M. Furuya, J. Ishida, S. Inaba, Y. Kasuya, S. Kimura, R. Nemori, A. Fukamizu, Impaired placental neovascularization in mice with pregnancy-associated hypertension. *Lab. Invest.* **88**, 416–429 (2008).
10. G. Bobek, T. Stait-Gardner, W. S. Price, A. Makris, A. Hennessy, Quantification of placental change in mouse models of preeclampsia using magnetic resonance microscopy. *Eur. J. Histochem.* **62**, 2868 (2018).
11. G. S. J. Whitley, J. E. Cartwright, Cellular and molecular regulation of spiral artery remodelling: Lessons from the cardiovascular field. *Placenta* **31**, 465–474 (2010).
12. L. Leach, J. A. Firth, Structure and permeability of human placental microvasculature. *Microsc. Res. Tech.* **38**, 137–144 (1997).
13. O. Genbacev, Y. Zhou, J. W. Ludlow, S. J. Fisher, Regulation of human placental development by oxygen tension. *Science* **277**, 1669–1672 (1997).
14. C. Errico, J. Pierre, S. Pezet, Y. Desailly, Z. Lenkei, O. Couture, M. Tanter, Ultrafast ultrasound localization microscopy for deep super-resolution vascular imaging. *Nature* **527**, 499–502 (2015).
15. S. Fekkes, A. E. Swillens, H. H. Hansen, A. E. Saris, M. M. Nillesen, F. Iannaccone, P. Segers, C. L. de Korte, 2D versus 3D cross-correlation-based radial and circumferential strain estimation using multiplane 2D ultrafast ultrasound in a 3D atherosclerotic carotid artery model. *IEEE Trans. Ultrason. Ferroelectr. Freq. Control* **63**, 1543–1553 (2016).
16. M. Flesch, M. Pernot, J. Provost, G. Ferin, A. Nguyen-Dinh, M. Tanter, T. Deffieux, 4D in vivo ultrafast ultrasound imaging using a row-column addressed matrix and coherently-compounded orthogonal plane waves. *Phys. Med. Biol.* **62**, 4571–4588 (2017).
17. V. Hingot, C. Errico, M. Tanter, O. Couture, Subwavelength motion-correction for ultrafast ultrasound localization microscopy. *Ultrasonics* **77**, 17–21 (2017).
18. E. Lugo-Hernandez, A. Squire, N. Hagemann, A. Brenzel, M. Sardari, J. Schlechter, E. H. Sanchez-Mendoza, M. Gunzer, A. Faissner, D. M. Hermann, 3D visualization and quantification of microvessels in the whole ischemic mouse brain using solvent-based clearing and light sheet microscopy. *J. Cereb. Blood Flow Metab.* **37**, 3355–3367 (2017).
19. M. Tanter, M. Fink, Ultrafast imaging in biomedical ultrasound. *IEEE Trans. Ultrason. Ferroelectr. Freq. Control* **61**, 102–119 (2014).
20. A. Kosareva, L. Abou-Elkacem, S. Chowdhury, J. R. Lindner, B. A. Kaufmann, Seeing the invisible-ultrasound molecular imaging. *Ultrasound Med. Biol.* **46**, 479–497 (2020).
21. S. Dekan, N. Linduska, G. Kasprian, D. Prayer, MRI of the placenta - a short review. *Wien. Med. Wochenschr.* **162**, 225–228 (2012).
22. R. M. Lewis, J. E. Pearson-Farr, Multiscale three-dimensional imaging of the placenta. *Placenta* **102**, 55–60 (2020).
23. D. Entenberg, S. Voiculescu, P. Guo, L. Borriello, Y. Wang, G. S. Karagiannis, J. Jones, F. Baccay, M. Oktay, J. Condeelis, A permanent window for the murine lung enables high-resolution imaging of cancer metastasis. *Nat. Methods* **15**, 73–80 (2018).
24. Q. Huang, M. A. Cohen, F. C. Alsina, G. Devlin, A. Garrett, J. McKey, P. Havlik, N. Rakhilin, E. Wang, K. Xiang, P. Mathews, L. Wang, C. Bock, V. Ruthig, Y. Wang, M. Negrete, C. W. Wong, P. K. L. Murthy, S. Zhang, A. R. Daniel, D. G. Kirsch, Y. Kang, B. Capel, A. Asokan, D. L. Silver, R. Jaenisch, X. Shen, Intravital imaging of mouse embryos. *Science* **368**, 181–186 (2020).
25. F. R. De Bie, M. G. Davey, A. C. Larson, J. Deprest, A. W. Flake, Artificial placenta and womb technology: Past, current, and future challenges towards clinical translation. *Prenat. Diagn.* **41**, 145–158 (2021).
26. L. V. Wang, J. Yao, A practical guide to photoacoustic tomography in the life sciences. *Nat. Methods* **13**, 627–638 (2016).
27. J. Yao, L. Wang, J. M. Yang, K. I. Maslov, T. T. Wong, L. Li, C. H. Huang, J. Zou, L. V. Wang, High-speed label-free functional photoacoustic microscopy of mouse brain in action. *Nat. Methods* **12**, 407–410 (2015).
28. J. Yao, K. I. Maslov, Y. Zhang, Y. Xia, L. V. Wang, Label-free oxygen-metabolic photoacoustic microscopy in vivo. *J. Biomed. Opt.* **16**, 076003 (2011).
29. J. Yao, J. Xia, K. I. Maslov, M. Nasiriavanaki, V. Tsytsarev, A. V. Demchenko, L. V. Wang, Noninvasive photoacoustic computed tomography of mouse brain metabolism in vivo. *Neuroimage* **64**, 257–266 (2013).
30. X. Zhu, Q. Huang, A. DiSpirito, T. Vu, Q. Rong, X. Peng, H. Sheng, X. Shen, Q. Zhou, L. Jiang, U. Hoffmann, J. Yao, Real-time whole-brain imaging of hemodynamics and oxygenation at micro-vessel resolution with ultrafast wide-field photoacoustic microscopy. *Light Sci. Appl.* **11**, 138 (2022).
31. B. Drews, L. F. Landaverde, A. Kühl, U. Drews, Spontaneous embryo resorption in the mouse is triggered by embryonic apoptosis followed by rapid removal via maternal sterile purulent inflammation. *BMC Dev. Biol.* **20**, 1 (2020).
32. Global Burden of Disease Study 2013 Collaborators, Study, Global, regional, and national incidence, prevalence, and years lived with disability for 301 acute and chronic diseases and injuries in 188 countries, 1990–2013: A systematic analysis for the Global Burden of Disease Study 2013. *Lancet* **386**, 743–800 (2015).
33. J. S. Abramowicz, E. Sheiner, In utero imaging of the placenta: Importance for diseases of pregnancy. *Placenta* **28**, S14–S22 (2007).
34. F. Lyall, S. C. Robson, J. N. Bulmer, Spiral artery remodeling and trophoblast invasion in preeclampsia and fetal growth restriction: Relationship to clinical outcome. *Hypertension* **62**, 1046–1054 (2013).
35. R. Pijnenborg, L. Vercruysse, M. Hanssens, The uterine spiral arteries in human pregnancy: Facts and controversies. *Placenta* **27**, 939–958 (2006).
36. P. P. Borowicz, D. R. Arnold, M. L. Johnson, A. T. Grazul-Bilska, D. A. Redmer, L. P. Reynolds, Placental growth throughout the last two thirds of pregnancy in sheep: Vascular development and angiogenic factor expression. *Biol. Reprod.* **76**, 259–267 (2007).
37. S. Aguree, A. D. Gernand, Plasma volume expansion across healthy pregnancy: A systematic review and meta-analysis of longitudinal studies. *BMC Pregnancy Childbirth* **19**, 508 (2019).
38. Y. Ma, Q. Yang, M. Fan, L. Zhang, Y. Gu, W. Jia, Z. Li, F. Wang, Y. X. Li, J. Wang, R. Li, X. Shao, Y. L. Wang, Placental endovascular extravillous trophoblasts (enEVTs) educate maternal T-cell differentiation along the maternal-placental circulation. *Cell Prolif.* **53**, e12802 (2020).
39. S. Kalkunte, Z. Lai, N. Tewari, C. Chichester, R. Romero, J. Padbury, S. Sharma, In vitro and in vivo evidence for lack of endovascular remodeling by third trimester trophoblasts. *Placenta* **29**, 871–878 (2008).
40. J. Patel, K. Landers, R. Mortimer, K. Richard, Regulation of hypoxia inducible factors (HIF) in hypoxia and normoxia during placental development. *Placenta* **31**, 951–957 (2010).
41. F. Wu, F.-J. Tian, Y. Lin, Oxidative stress in placenta: Health and diseases. *Biomed. Res. Int.* **2015**, 293271 (2015).
42. G. J. Burton, Oxygen, the Janus gas; Its effects on human placental development and function. *J. Anat.* **215**, 27–35 (2009).
43. S. Oladipupo, S. Hu, J. Kovalski, J. J. Yao, A. Santeford, R. E. Sohn, R. Shohet, K. Maslov, L. H. V. Wang, J. M. Arbeit, VEGF is essential for hypoxia-inducible factor-mediated neovascularization but dispensable for endothelial sprouting. *Proc. Natl. Acad. Sci. U.S.A.* **108**, 13264–13269 (2011).
44. Y. Liu, Y. Balaraman, G. Wang, K. P. Nephew, F. C. Zhou, Alcohol exposure alters DNA methylation profiles in mouse embryos at early neurulation. *Epigenetics* **4**, 500–511 (2009).
45. C. Kiecker, The chick embryo as a model for the effects of prenatal exposure to alcohol on craniofacial development. *Dev. Biol.* **415**, 314–325 (2016).
46. G. Duester, Alcohol dehydrogenase as a critical mediator of retinoic acid synthesis from vitamin A in the mouse embryo. *J. Nutr.* **128**, 459S–462S (1998).
47. S. M. Smith, Alcohol-induced cell death in the embryo. *Alcohol Health Res. World* **21**, 287–297 (1997).
48. C. Bosco, E. Diaz, Placental hypoxia and foetal development versus alcohol exposure in pregnancy. *Alcohol Alcohol.* **47**, 109–117 (2012).
49. S. H. Poodeh, T. Salonurmi, I. Nagy, P. Koivunen, J. Vuoristo, J. Räsänen, R. Sormunen, S. Vainio, M. Savolainen, Alcohol-induced premature permeability in mouse placenta-yolk sac barriers in vivo. *Placenta* **33**, 866–873 (2012).
50. M. Turan Akay, E. Arzu Koçkaya, The effects of alcohol on rat placenta. *Cell Biochem. Funct.* **23**, 435–445 (2005).
51. O. Garcia-Algar, L. Carballo, N. Reguart, J. Salat-Batlle, Neurobehavioural effects of prenatal exposure to alcohol. *J. Preg. Child. Health* **02**, 177 (2015).

52. P. A. May, J. P. Gossage, Estimating the prevalence of fetal alcohol syndrome. *A summary. Alcohol Res Health* **25**, 159–167 (2001).
53. J. O. Lo, M. C. Schabel, V. H. Roberts, X. Wang, K. S. Lewandowski, K. A. Grant, A. E. Frias, C. D. Kroenke, First trimester alcohol exposure alters placental perfusion and fetal oxygen availability affecting fetal growth and development in a non-human primate model. *Am. J. Obstet. Gynecol.* **216**, 302.e1–302.e8 (2017).
54. J. O. Lo, M. C. Schabel, V. H. J. Roberts, T. K. Morgan, S. S. Fei, L. Gao, K. G. Ray, K. S. Lewandowski, N. P. Newman, J. A. Bohn, K. A. Grant, A. E. Frias, C. D. Kroenke, Effects of early daily alcohol exposure on placental function and fetal growth in a rhesus macaque model. *Am. J. Obstet. Gynecol.* **226**, 130.e1–130.e11 (2022).
55. D. J. Livy, S. E. Parnell, J. R. West, Blood ethanol concentration profiles: A comparison between rats and mice. *Alcohol* **29**, 165–171 (2003).
56. J. B. Freund, M. Orescanin, Cellular flow in a small blood vessel. *J. Fluid Mech.* **671**, 466–490 (2011).
57. E. Kasterstein, D. Strassburger, D. Komarovsky, O. Bern, A. Komsky, A. Raziel, S. Friedler, R. Ron-El, The effect of two distinct levels of oxygen concentration on embryo development in a sibling oocyte study. *J. Assist. Reprod. Genet.* **30**, 1073–1079 (2013).
58. P. A. Dennery, Effects of oxidative stress on embryonic development. *Birth Defects Res. C Embryo Today* **81**, 155–162 (2007).
59. M. Killion, Cardiac arrest in pregnancy. *MCN Am. J. Matern. Child. Nurs.* **40**, 262 (2015).
60. J. Kikuchi, S. Deering, Cardiac arrest in pregnancy. *Semin. Perinatol.* **42**, 33–38 (2018).
61. T. A. Bennett, V. L. Katz, C. M. Zelop, Cardiac arrest and resuscitation unique to pregnancy. *Obstet. Gynecol. Clin. North Am.* **43**, 809–819 (2016).
62. R. Li, W. Duan, D. Zhang, U. Hoffmann, J. Yao, W. Yang, H. Sheng, Mouse cardiac arrest model for brain imaging and brain physiology monitoring during ischemia and resuscitation. *J Vis Exp*, e65340 (2023).
63. C. M. Zelop, S. Einav, J. M. Mhyre, S. Martin, Cardiac arrest during pregnancy: Ongoing clinical conundrum. *Am. J. Obstet. Gynecol.* **219**, 52–61 (2018).
64. A. Gilman-Sachs, S. Dambaeva, M. D. S. Garcia, Y. Hussein, J. Kwak-Kim, K. Beaman, Inflammation induced preterm labor and birth. *J. Reprod. Immunol.* **129**, 53–58 (2018).
65. T. Yan, K. Cui, X. Huang, S. Ding, Y. Zheng, Q. Luo, X. Liu, L. Zou, Assessment of therapeutic efficacy of miR-126 with contrast-enhanced ultrasound in preeclampsia rats. *Placenta* **35**, 23–29 (2014).
66. Y. Zhang, T. Le, R. Grabau, Z. Mohseni, H. Kim, D. R. Natale, L. Feng, H. Pan, H. Yang, TMEM16F phospholipid scramblase mediates trophoblast fusion and placental development. *Sci. Adv.* **6**, eaba0310 (2020).
67. J. Zhang, S. Jing, H. Zhang, J. Zhang, H. Xie, L. Feng, Low-dose aspirin prevents LPS-induced preeclampsia-like phenotype via AQP-1 and the MAPK/ERK 1/2 pathway. *Placenta* **121**, 61–69 (2022).
68. G. T. Knipp, K. L. Audus, M. J. Soares, Nutrient transport across the placenta. *Adv. Drug Deliv. Rev.* **38**, 41–58 (1999).
69. E. Delorme-Axford, Y. Sadovsky, C. B. Coyne, The placenta as a barrier to viral infections. *Annu. Rev. Virol.* **1**, 133–146 (2014).
70. A. Gil, R. Rueda, S. E. Ozanne, E. M. van der Beek, C. van Loo-Bouwman, M. Schoemaker, V. Marinello, K. Venema, C. Stanton, B. Schelkle, Is there evidence for bacterial transfer via the placenta and any role in the colonization of the infant gut?–a systematic review. *Crit. Rev. Microbiol.* **46**, 493–507 (2020).
71. S. Lager, T. L. Powell, Regulation of nutrient transport across the placenta. *J. Pregnancy* **2012**, 179827 (2012).
72. N. Tetro, S. Moushaev, M. Rubinchik-Stern, S. Eyal, The placental barrier: The gate and the fate in drug distribution. *Pharm. Res.* **35**, 71 (2018).
73. M. A. Kotterman, D. V. Schaffer, Engineering adeno-associated viruses for clinical gene therapy. *Nat. Rev. Genet.* **15**, 445–451 (2014).
74. H. Büning, L. Perabo, O. Coutelle, S. Quadt-Humme, M. Hallek, Recent developments in adeno-associated virus vector technology. *J. Gene. Med.* **10**, 717–733 (2008).
75. K. Vähäkangas, P. Myllynen, Drug transporters in the human blood-placental barrier. *Br. J. Pharmacol.* **158**, 665–678 (2009).
76. G. Wu, F. W. Bazer, J. M. Wallace, T. E. Spencer, Board-invited review: Intrauterine growth retardation: Implications for the animal sciences. *J. Anim. Sci.* **84**, 2316–2337 (2006).
77. L. V. Wang, S. Hu, Photoacoustic tomography: In vivo imaging from organelles to organs. *Science* **335**, 1458–1462 (2012).
78. J. Yao, L. V. Wang, Photoacoustic microscopy. *Laser. Photon. Rev.* **7**, 758–778 (2013).
79. Y. Afshar, J. Dong, P. Zhao, L. Li, S. Wang, R. Y. Zhang, C. Zhang, O. Yin, C. S. Han, B. D. Einerson, T. L. Gonzalez, H. Zhang, A. Zhou, Z. Yang, S. J. Chou, N. Sun, J. Cheng, H. Zhu, J. Wang, T. X. Zhang, Y. T. Lee, J. J. Wang, P. C. Teng, P. Yang, D. Qi, M. Zhao, M. S. Sim, R. Zhe, J. D. Goldstein, J. Williams III, X. Wang, Q. Zhang, L. D. Platt, C. Zou, M. D. Pisarska, H. R. Tseng, Y. Zhu, Circulating trophoblast cell clusters for early detection of placenta accreta spectrum disorders. *Nat. Commun.* **12**, 4408 (2021).
80. J. R. Bumstead, J. J. Park, I. A. Rosen, A. W. Kraft, P. W. Wright, M. D. Reisman, D. C. Cote, J. P. Culver, Designing a large field-of-view two-photon microscope using optical invariant analysis. *Neurophotonics* **5**, 025001 (2018).

Acknowledgments: We thank L. Cameron (Duke University) for assistance with two-photon microscopy. We also thank J. Everitt (Duke University) for pathology examination of the placenta staining. **Funding:** The work is supported by the National Institutes of Health (NIH) (RF1NS115581 (BRAIN Initiative), R01NS111039, R01EB028143), National Science Foundation CAREER award 2144788, and Chan Zuckerberg Initiative Grant 2020-226178 (to J.Y); and by NSF C81670468, 2017KJXX-43, 2018SF-208 (to Q.H.); as well as by NIH R01DK132889, R35GM122465, and DK119795 (to X.S.). **Author contributions:** Q.H., X.Z., X.S., and J.Y. conceived the idea. Q.H. and X.Z. designed the materials and methods. X.Z., Q.H., and L.J. prepared the materials and conducted material characterizations. X.Z. developed the imaging systems with assistance from Q.R., T.V., L.J. and Q.Z. L.J. developed the transducers. X.Z. and Q.H. performed the experiments with assistance from L.J., G.D., J.S., V.-T.N., X.W., Y.C., L.M., K.X., E.W., Q.R., T.V., Q.Z., L.F., Y.K., A.A., and S.-W.D.H. X.Z. and Q.H. analyzed the results. X.Z., Q.H., L.F., and J. Y. wrote the manuscript with input from all the authors. Q.H., X.S., and J.Y. supervised the study. **Competing interests:** X.S. is a co-founder of Xilis Inc. This manuscript does not have any overlap with Xilis's commercial interests. All other authors declare that they have no competing interests. **Data and materials availability:** All data needed to evaluate the conclusions in the paper are present in the paper and/or the Supplementary Materials. Computer codes for image analysis are provided on Zenodo (https://doi.org/10.5281/zenodo.10652260).

Submitted 3 August 2023
Accepted 16 February 2024
Published 20 March 2024
10.1126/sciadv.adk1278